JCB Journal of Cell Biology

REPORT

Somatic polyploidy supports biosynthesis and tissue function by increasing transcriptional output

Alexander T. Lessenger[1], Jan M. Skotheim[1,2], Mathew P. Swaffer[1,3], and Jessica L. Feldman[1]

Cell size and biosynthetic capacity generally increase with increased DNA content. Somatic polyploidy has therefore been proposed to be an adaptive strategy to increase cell size in specialized tissues with high biosynthetic demands. However, if and how DNA concentration limits cellular biosynthesis in vivo is not well understood. Here, we show that polyploidy in the *Caenorhabditis elegans* intestine is critical for cell growth and yolk biosynthesis, a central role of this organ. Artificially lowering the DNA/cytoplasm ratio by reducing polyploidization in the intestine gave rise to smaller cells with dilute mRNA. Highly expressed transcripts were more sensitive to this mRNA dilution, whereas lowly expressed genes were partially compensated—in part by loading more RNA Polymerase II on the remaining genomes. Polyploidy-deficient animals produced fewer and slower-growing offspring, consistent with reduced synthesis of highly expressed yolk proteins. DNA-dilute cells had normal total protein concentration, which we propose is achieved by increasing the expression of translational machinery at the expense of specialized, cell-type–specific proteins.

Introduction

Proliferating cells coordinate DNA replication with growth to maintain the ratio between the genome and cytoplasm volume. In the absence of DNA replication, the genome is diluted by cell growth, leading to biosynthetic collapse in extreme cases (Neurohr et al., 2019). Many organisms have adapted strategies to overcome this apparent limitation on cell size (Marshall et al., 2012; O'Farrell, 2015) such as polyploidization, the process of generating >2 copies of the genome per cell. Most multicellular organisms have polyploid cell types, which arise during normal development by converting a mitotic cell cycle into an endocycle where DNA is replicated without subsequent cell division or by the fusion of many cells into a single syncytium (Edgar et al., 2014). These events are often developmentally programmed, such as in the insect salivary gland, mammalian liver, and plant leaf epidermis (Dej and Spradling, 1999; Roeder et al., 2012; Gentric and Desdouets, 2014). Several studies have shown that increased DNA content causally increases cell size (Unhavaithaya and Orr-Weaver, 2012; Hansson et al., 2020; Ma et al., 2022; Darmasaputra et al., 2024), thus polyploidization may enable an accompanied increase in biosynthetic capacity, but such a requirement has never been tested in vivo.

A role for DNA content in facilitating rapid biosynthesis in multicellular organisms would be consistent with work from proliferating, single-celled systems, where the growth rate decreases as the genome dilutes (Neurohr et al., 2019). Proteins and transcripts change in concentration as the cell grows, but the proteomic and transcriptomic signatures of large cells are eliminated upon genome duplication (Neurohr et al., 2019; Chen et al., 2020; Lanz et al., 2022; Swaffer et al., 2023). This result, and the observation that polyploidization in cultured lymphocytic leukemia cells permits a normal growth rate well beyond normal size (Mu et al., 2020), shows that these effects are due to the reduction of the DNA/cytoplasm ratio, not cell size per se. However, differentiated cells face substantially different pressures from single cells in culture that maximize their growth and division rates, and thus whether these studies can be extrapolated to cells in multicellular organisms remains to be tested.

A major gap in our understanding is how DNA content mechanistically limits growth and biosynthesis. One possibility, identified in budding yeast, is that the concentrations of both RNA Polymerase II (Pol II) and the genome are limiting for mRNA transcription (Swaffer et al., 2023). However, only the few most highly expressed gene promoters may be near saturation, indicating that most genes have substantial capacity to load more polymerase and increase transcription (Swaffer et al., 2023). Thus, we hypothesize that only a few transcripts reach a ploidy-imposed transcription limit and that other transcripts scale their production accordingly.

[1]Department of Biology, Stanford University, Stanford, CA, USA; [2]Chan-Zuckerberg Biohub, San Francisco, CA, USA; [3]Wellcome Centre for Cell Biology, University of Edinburgh, Edinburgh, UK.

Correspondence to Jessica L. Feldman: feldmanj@stanford.edu; Mathew P. Swaffer: matthew.swaffer@ed.ac.uk.

The intestine of the nematode worm *Caenorhabditis elegans* offers an excellent model to test the importance of DNA content in vivo as it is a polyploid tissue with high biosynthetic capacity in a genetically tractable, multicellular organism. During normal *C. elegans* development, the intestine becomes polyploid through a series of programmed endocycles that are coordinated with progression through larval stages (Fig. 1 A; Hedgecock and White, 1985). In addition to its role in nutrient absorption and storage, the adult hermaphrodite intestine synthesizes an enormous amount of yolk protein, which is shuttled to oocytes and aids in larval development of progeny (Van Rompay et al., 2015; Perez and Lehner, 2019).

We limited polyploidization of the intestine using tissue- and time-specific disruption of the cell cycle, allowing us to directly test the necessity of polyploidy for a variety of physiological functions, including cell and organelle size and the synthesis of yolk and other molecules. We demonstrate that polyploidy in the intestine is necessary for large cell size but is not limited to the final body size. Tissue-specific RNA-sequencing (RNA-seq) and Pol II Chromatin immunoprecipitation (ChIP)-seq experiments revealed that reduced ploidy causes a global reduction in the expression of all genes but has a more severe effect on the most highly expressed genes. Finally, we show that polyploidy is required for efficient yolk biosynthesis and rapid development of progeny. Together, our data identify how biological molecules scale with a changing DNA/cytoplasm ratio in a multicellular, differentiated context, and demonstrate that polyploidy is a critical strategy for increasing biosynthetic capacity.

Results and discussion

Intestine-specific depletion of CDK-2 disrupts polyploidization in the *C. elegans* intestine

Polyploidy arises during the normal and stereotyped development of the *C. elegans* intestine. During embryogenesis, cell divisions increase intestinal cell number from 1 to 20 and total DNA content from 2C to 40C (C = 1 haploid genome). During larval development, most of these cells undergo endomitosis to become binucleated, followed by several rounds of endoreduplication that increase the ploidy of all individual nuclei from 2C to 32C and of the whole organ to 1,024C (Fig. 1 A; Hedgecock and White, 1985).

To modify intestinal ploidy, we degraded the G1-S promoting cyclin-dependent kinase (CDK) CDK-2 using the ZIF-1/ZF protein degradation system (Armenti et al., 2014; Sallee et al., 2018). CDK-2 was endogenously tagged with a zinc finger degron (ZF), and a degrader (ZIF-1) was expressed in the intestine from the *asp-1p* promoter, which begins expression before binucleation but after the final intestinal cell divisions (Fig. 1 B). Worms with degraded intestinal CDK-2 (CDK-2$^{gut(-)}$) are the F1 homozygous progeny of balanced heterozygotes unless otherwise indicated (Fig. 1 C).

We found that CDK-2 degradation nearly eliminated endomitosis but did not affect cell division, decreasing the total nucleus number from 31.3 in control to 22.9, on average (Fig. 1, D and E). To determine whether CDK-2$^{gut(-)}$ worms had reduced DNA content in intestinal nuclei, we quantified the total fluorescence intensity of nuclei after staining with Hoechst, relative to neighboring tetraploid pachytene germline nuclei in the same worm. CDK-2$^{gut(-)}$ animals were fertile and produced viable progeny, indicating germline ploidy was unaffected. Average intestinal nucleus ploidy was reduced from 32.3C in control worms to 6.4C in CDK-2$^{gut(-)}$ worms (Fig. 1, F and G), with most nuclei being ~4 or 8C. We noted that this and many of our subsequent analyses were restricted to the anterior intestine for technical reasons (see Materials and methods). From the reduction in nucleus number and ploidy, we estimated that CDK-2$^{gut(-)}$ intestines have a total DNA content of 134C, 13% of the control.

Polyploidy promotes larger cell size in several contexts, so we measured the size of the overall intestine and of individual cells following ploidy reduction. We found that adult CDK-2$^{gut(-)}$ intestines were 66% the size of control due to decreased width (Fig. 1, H and I; and Fig. S1), indicating that DNA content limits cell size in our system. Because CDK-2 depletion decreased DNA content more than cell size, the DNA concentration in the intestine was diluted to 21% of control: from 825 C/nl in control to 169 C/nl in CDK-2$^{gut(-)}$ worms (Fig. 1 J). Thus, each copy of the genome in CDK-2$^{gut(-)}$ intestines supports a greater volume of cytoplasm, enabling cells to grow beyond their normal DNA/cytoplasm ratio and resulting in DNA-dilute cells. Together, these data show that intestine-specific depletion of CDK-2 severely limits DNA content and can therefore serve as a model to test the importance of high ploidy in this tissue.

Global increase in mRNA per genome buffers the effects of reduced ploidy

In budding yeast, DNA dilution causes RNA dilution (Neurohr et al., 2019), and we wanted to see if this relationship also held in the *C. elegans* intestine. We measured global mRNA concentration by performing fluorescence in situ hybridization against the poly-A tail of mRNA (poly(A)-FISH) and found that the cellular concentration of mRNA was reduced in CDK-2$^{gut(-)}$ intestines relative to the neighboring germline of the same worm (Fig. 2, A and B). However, this reduction in mRNA concentration (76% of control) was far less than the reduction in DNA concentration (21% of control), revealing that active compensation mechanisms increase the number of transcripts supported by each genome. One such mechanism identified in budding yeast is an increase in Pol II abundance, which explains how transcription rates increase in larger yeast cells (Swaffer et al., 2023). To determine whether Pol II abundance similarly increased in DNA-dilute intestinal cells, we measured the amount of endogenously tagged Pol II (AMA-1::GFP) in the intestines of live worms. Consistent with prior work showing nucleus size and total Pol II amount scale with cell size (Cantwell and Nurse, 2019; Swaffer et al., 2023), we found that total nuclear volume and Pol II amount within a cell decreased in proportion with the cell size reduction in CDK-2$^{gut(-)}$ intestines (Fig. 2, D–G). The maintenance of nuclear Pol II concentration in these DNA-dilute cells increased the Pol II-to-DNA ratio by 4.2-fold, which is expected to increase transcription from each genome. Further, nuclear

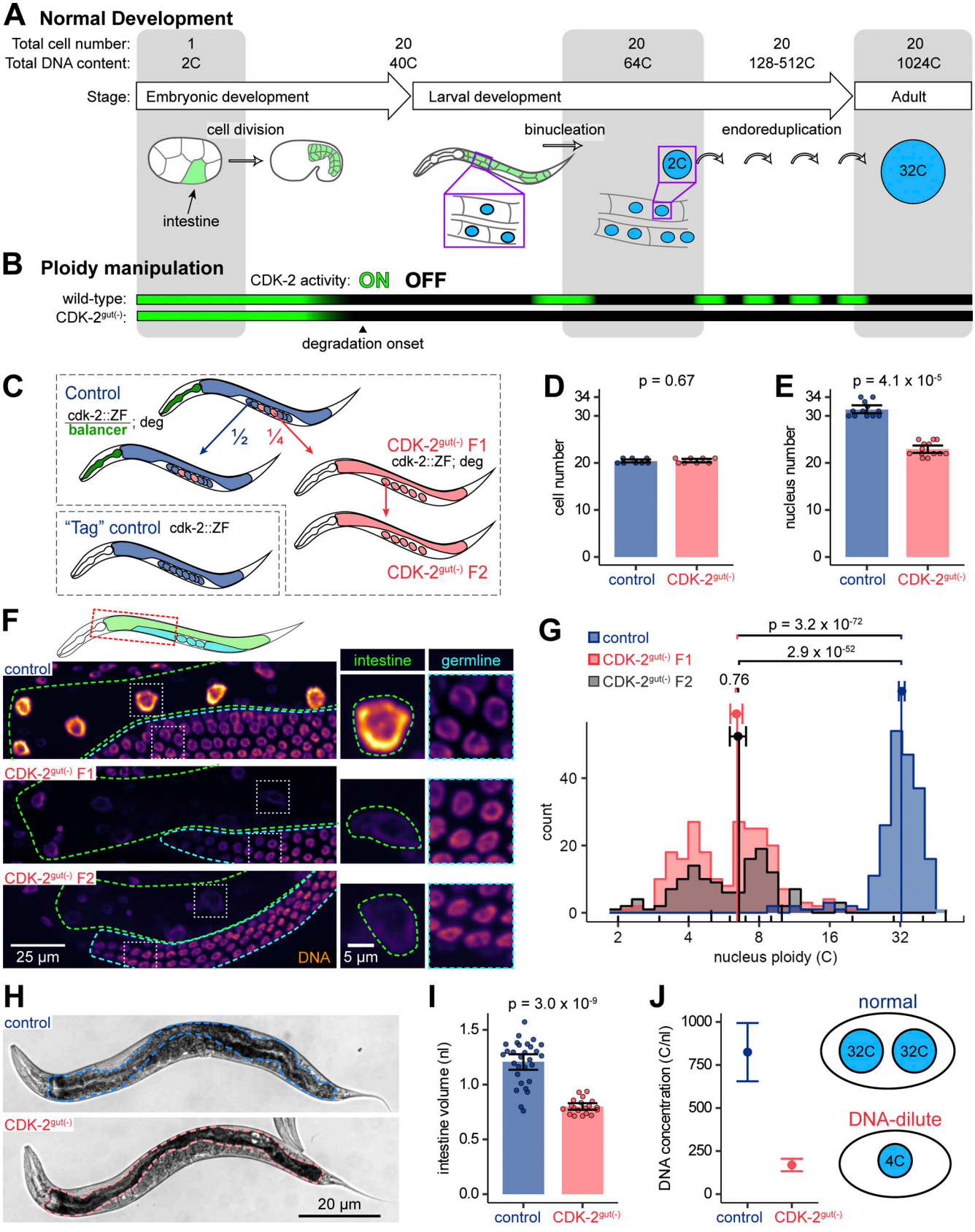

Figure 1. **A tool to disrupt polyploidization. (A)** Cartoon depicting *C. elegans* intestinal development, the origins of polyploidy in this tissue, and the cell numbers and ploidy values at each developmental stage. **(B)** Cartoon depicting timing of intestine-specific CDK-2 degradation and timing of CDK-2 activity in wild-type and CDK-2$^{gut(-)}$ intestines. **(C)** Cartoon depicting genetics of experimental and control strains. **(D)** Quantification of intestinal nucleus number in L1

worms, representing final cell number. **(E)** Quantification of intestinal nucleus number in L4 worms, representing final nucleus number. **(F)** Sum projections of 3D images of day 1 adult worms fixed and stained with Hoechst DNA-binding dye (viridis-inferno coloring). Insets show nuclei from the third intestinal ring and neighboring pachytene germline cells. **(G)** Quantification of nucleus ploidy in control and CDK-2$^{gut(-)}$ F1 and F2 day 1 adult intestines. Dots and error bars represent means and 95% confidence interval. Kruskal–Wallis test P = 6.6 × 10^{-85}; P values shown are from post-hoc Dunn test with Benjamini-Hochberg multiple hypothesis testing correction. **(H)** Representative DIC images of live adult control and CDK- 2$^{gut(-)}$ worms. Intestines are outlined in blue (control) or red (CDK-2$^{gut(-)}$) dotted lines. Worms are age-matched at 96 h post-egg lay. **(I)** Quantification of intestine volume, estimated from length and cross-sectional area. Each point represents one worm. In D, E, and I, bars and error bars represent means and 95% confidence intervals; P values are from Mann–Whitney U tests. **(J)** Left: Estimation of DNA/cytoplasm ratio in control and CDK-2$^{gut(-)}$ intestines from parameters in D–I. Error bars represent combined standard deviation. Right: Cartoon depicting normal and DNA-dilute cells.

mRNA decreased in CDK-2$^{gut(-)}$ intestines (Fig. 2 C), which has been proposed to increase global transcription efficiency in cell culture (Berry et al., 2022). These data are consistent with a model where mRNA synthesis rates are increased in CDK-2$^{gut(-)}$ intestines, although we were unable to measure these rates directly.

Highly expressed transcripts are more sensitive to DNA limitation

Based on our observation that mRNA levels per genome globally increase in DNA-dilute cells, we next sought to understand how DNA dilution affects the expression of individual genes by conducting a modified RNA-seq experiment that could detect

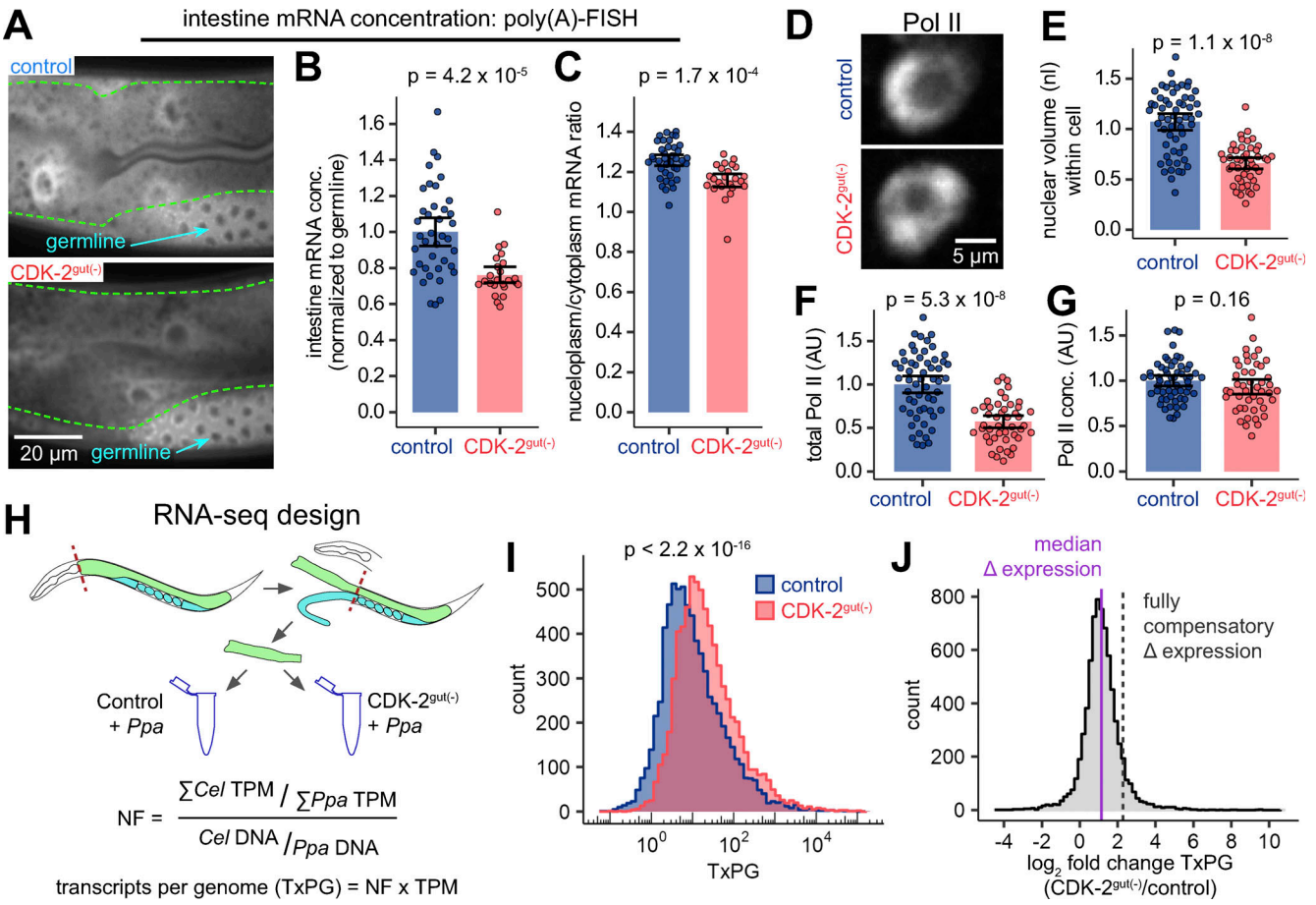

Figure 2. **mRNA abundance is partially limited by DNA content in the intestine. (A)** Confocal images of FISH against poly(A) tails in int2–int3 intestine rings of control and CDK-2$^{gut(-)}$ worms. **(B)** Quantification of cytoplasmic mRNA concentration in int2–int4 intestine rings from images as in A. **(C)** Quantification of the ratio of the nucleoplasmic mRNA to the cytoplasmic mRNA from images as in A. In B and C, each dot represents one worm. **(D)** Live confocal images of intestinal nuclei of day 1 adult worms expressing endogenously-tagged Pol II (AMA-1::GFP). **(E–G)** Quantification of the total volume (E), total amount (F, total fluorescence intensity), and concentration (G, mean fluorescence intensity) of AMA-1 in int2–int4 cells. Volume and total intensity measurements of individual nuclei were summed in binucleate cells. Each dot represents one cell. In B, C, and E–G, bars and error bars represent means and 95% confidence intervals; P values are from Mann-Whitney U tests after Benjamini-Hochberg multiple hypothesis testing correction. **(H)** Cartoon depicting normalized RNA-seq experiment: dissected intestines from two species were mixed, and *C. elegans* gene expression was normalized to the spike-in species, *P. pacificus*. **(I)** Distribution of transcripts per genome (TxPG) across all genes in control and CDK-2$^{gut(-)}$ intestines. P value is from *t* test after log transformation of TxPG values. **(J)** Distribution of changes in TxPG of all genes. The solid purple line represents the median change (Δ) in expression, and dashed black line indicates the level of expression change that would be necessary to fully restore normal mRNA concentration (1/ploidy reduction).

shifts in absolute RNA abundance. In standard RNA-seq methods, the measured abundance of a transcript is only meaningful in relation to other transcripts in the same sample, so we added a biological "spike-in" to enable a direct comparison of absolute transcript concentration between samples. To each sample of dissected *C. elegans* intestines, we added equal amounts of dissected intestines of the related nematode *Pristionchus pacificus* as a spike-in. We calculated the global ratio of *C. elegans* to *P. pacificus* transcripts and then divided this ratio by the *C. elegans* to *P. pacificus* DNA ratio determined by qPCR. This normalization factor gives the relative ratio of total mRNA per genome in each sample, which can then be multiplied by the gene-specific quantification for each transcript (transcripts per million, TPM) to give a relative expression of the total number of transcripts per genome (Fig. 2 H). While a fivefold increase in transcripts per genome in CDK-2$^{gut(-)}$ intestines would be needed to fully compensate for the reduced DNA concentration (21% of control, Fig. 1 J), we found that genes only increased transcripts per genome by a median of 2.14-fold (Fig. 2, I and J). This analysis corroborated our finding by poly(A)-FISH that DNA dilute cells increase RNA levels per genome but still have dilute mRNA.

How could the productivity of each genome increase? One possible model is that all genes compensate for limited DNA content by increasing transcription at a level inversely proportional to the level of DNA limitation (Fig. 3, A and B, "perfect compensation" model, light red). Alternatively, the degree of compensation may depend on initial gene expression levels (Fig. 3, A and B, "expression-dependent" model, dark red) if high Pol II occupancy on the promoters of highly expressed genes slows additional Pol II loading (Swaffer et al., 2023), causing more highly expressed transcripts to decrease in abundance relative to control. Consistent with the expression-dependent compensation model, we found that the increase in transcripts per genome in CDK-2$^{gut(-)}$ intestines decreased with increasing expression level (Fig. 3 C and Fig. S2 A), ruling out a model where limiting DNA template affects all transcripts equally. This phenotype mimics the downregulation of highly expressed genes in transcriptionally burdened yeast, suggesting the presence of a conserved buffering mechanism (Metzl-Raz et al., 2020). This effect may be caused by the activation of stress response genes, which are typically expressed at low levels, or by the altered expression of cell cycle–related genes. However, the removal of either of these sets of genes from our analysis did not change the relationship (Fig. S2 B). Notably, our results do not imply a strict threshold for DNA limitation, below which increasing transcription perfectly compensates for a limited DNA template. Instead, we observed a continuous decrease in compensation from lowly expressed to highly expressed genes.

Differential impact of ploidy on highly and lowly expressed genes can be only partly explained by RNA Polymerase II recruitment

We next wanted to determine whether the surprisingly high mRNA abundance in CDK-2$^{gut(-)}$ intestines was achieved by increasing transcription rates or mRNA stability. RNA-seq is a measurement of RNA abundance and so cannot distinguish between these models. To estimate the contribution of transcription rates, we performed a ChIP-seq experiment to quantify the amount of Pol II occupancy on promoters and gene bodies specifically in the intestine. We expressed a GFP nanobody in the adult intestine from the *vit-5p* promoter in worms with endogenously tagged Pol II/AMA-1::GFP (Fig. 3 D). After crosslinking, we pulled down the nanobody to enrich for complexes of DNA, Pol II::GFP, and nanobody, which should only form in intestinal cells. We quantified the occupancy of Pol II on gene bodies and transcription start sites, finding that these metrics were well correlated (Fig. S2, C and D), and indicating that there were no gross changes in initiation rates. However, we found a weak correlation between Pol II occupancy and expression level, and our genotypes were not resolved as well by Pol II ChIP-seq as by RNA-seq, likely due to the low signal achieved by our tripartite ChIP system (Fig. S2, E–G). Despite this limitation, we found that more highly expressed genes were indeed relatively less occupied by Pol II in CDK-2$^{gut(-)}$ intestines (Fig. 3 E; and Fig. S2, H and I). This result is consistent with a model where Pol II saturation kinetics explain why highly expressed genes are more sensitive to DNA dilution. However, this model predicts that highly occupied genes will have a lower increase in occupancy when DNA is limited, which we did not observe (Fig. S2 J). Thus, while there may be some gene-specific effect of transcript abundance on transcript synthesis, the observed expression-dependent effects may be better explained by changes in mRNA turnover rates such that lowly expressed transcripts are preferentially stabilized when DNA is diluted.

Protein concentrations are buffered in low ploidy cells despite reduced mRNA concentrations

To determine whether further compensation mechanisms buffer protein levels in DNA dilute cells, we estimated total protein concentration in fixed worms with a protein-binding dye (NHS-ester). Surprisingly, we found that the concentration of protein in the cytoplasm was unchanged between control and CDK-2$^{gut(-)}$ intestines, relative to the neighboring germline (Fig. 4, A and B). We corroborated this finding by measuring the abundance of several model proteins: intestine-specific NLS-mScarlet and endogenously tagged Pol II and Fibrillarin/FIB-1, which we found unchanged between control and CDK-2$^{gut(-)}$ intestines (Fig. 2 G and Fig. S3).

To understand how protein concentration can be kept constant when global mRNA concentrations are reduced, we investigated whether genes encoding translational machinery were upregulated in our RNA-seq dataset. As an unbiased approach, we calculated an enrichment score for each gene ontology (GO) annotation that identifies annotations whose member genes are, as a group, more or less abundant compared with the global distribution (Cox and Mann, 2012). Consistent with the hypothesis that CDK-2$^{gut(-)}$ intestines compensate for limited mRNA concentration by increasing translation, we found genes involved in translation to be significantly upregulated (Fig. 4 C, orange). Despite the increase in mRNA per genome, we found terms related to transcription (Fig. 4 C, green) were not uniformly upregulated, consistent with a regime in which DNA content is much more limiting for transcription than

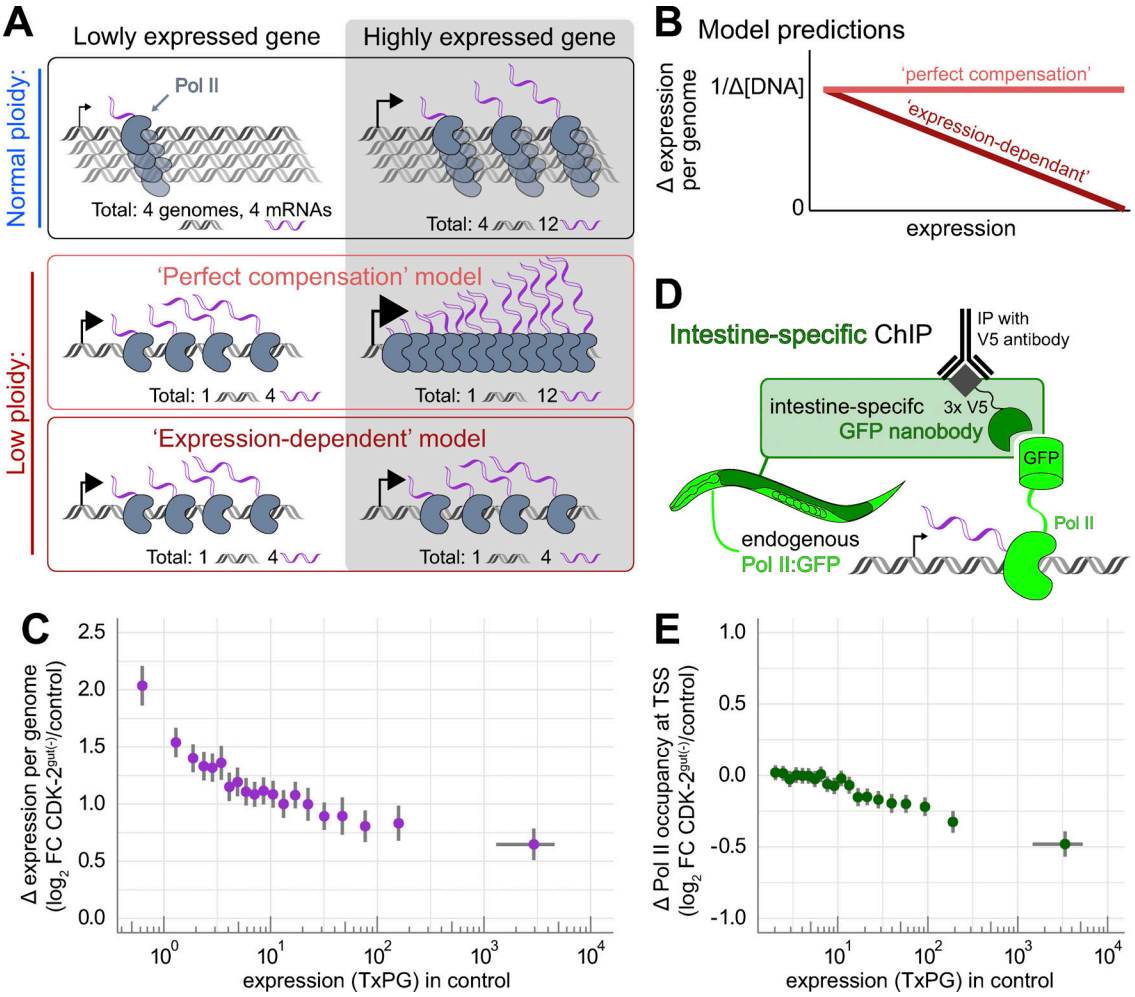

Figure 3. **Highly expressed mRNAs are more limited by DNA content. (A)** Cartoon depicting two models of transcriptional compensation for limited DNA content. **(B)** Mock data depicting how each model in A predicts how transcript abundance relative to genome copy number would change with increasing transcript abundance. **(C)** Change in spike-in normalized gene expression (TxPG) plotted against and binned by expression level in control, each bin represents 5% of genes. **(D)** Cartoon depicting experimental design for intestine-specific ChIP of Pol II. **(E)** Change in Pol II occupancy at the transcription start site (TSS) plotted against and binned by expression level in control, each bin represents 5% of genes. Colored dots in C and E represent mean fold change within the bin and error bars represent a 99% confidence interval.

Pol II. From this analysis, we also found a strong upregulation of nucleosome genes (Fig. 4 C, lavender), which was surprising because histones, their main protein component, typically scale with DNA content (Claude et al., 2021; Swaffer et al., 2021). The divergence in the behavior of transcripts encoding transcriptional versus translational machinery was even more clearly seen after accounting for their relative expression levels: we regressed the fold change in transcripts per genome to the log of the expression level with a polynomial regression ($R^2 = 0.091$, $p = 2.2 \times 10^{-16}$) and found that the residual change of ribosome subunits was significantly increased relative to those of Pol II and general transcription factors, or of all cytoplasmic genes (Fig. 4 D).

We hypothesized that increased expression of translational machinery would lead to increased ribosome concentration, which could buffer protein concentration against reduced global mRNA levels. Therefore, we measured the volume of the nucleolus and the abundance of the pre-rRNA processing protein, Fibrillarin/FIB-1, both of which have been shown to correlate with ribosome production (Frank and Roth, 1998; Lee et al., 2012; Yi et al., 2015; Uppaluri et al., 2016). We found that the total amount of FIB-1 per nucleolus was unchanged in CDK-2$^{gut(-)}$ intestines, but its local concentration increased due to these cells having proportionally smaller nucleoli (Fig. S3, B–E).

To estimate ribosome abundance more directly, we measured the change in ribosomal RNA (rRNA) and ribosomal protein subunits of the small complex RPS-5 and RPS-6. Genome-normalized rRNA levels measured by qPCR were increased in CDK-2$^{gut(-)}$ intestines relative to control (Fig. 4 E), predicting that CDK-2$^{gut(-)}$ intestines have a ribosome concentration that is 38% of control, despite the fivefold reduction in DNA concentration. We saw a similar buffering in RPS-5 levels measured by western blot in dissected intestines of control and CDK-2$^{gut(-)}$ worms. Normalizing RPS-5 intensity to the total protein in the sample revealed that the fraction of the proteome dedicated to RPS-5 was decreased in CDK-2$^{gut(-)}$ intestines to 50% of control

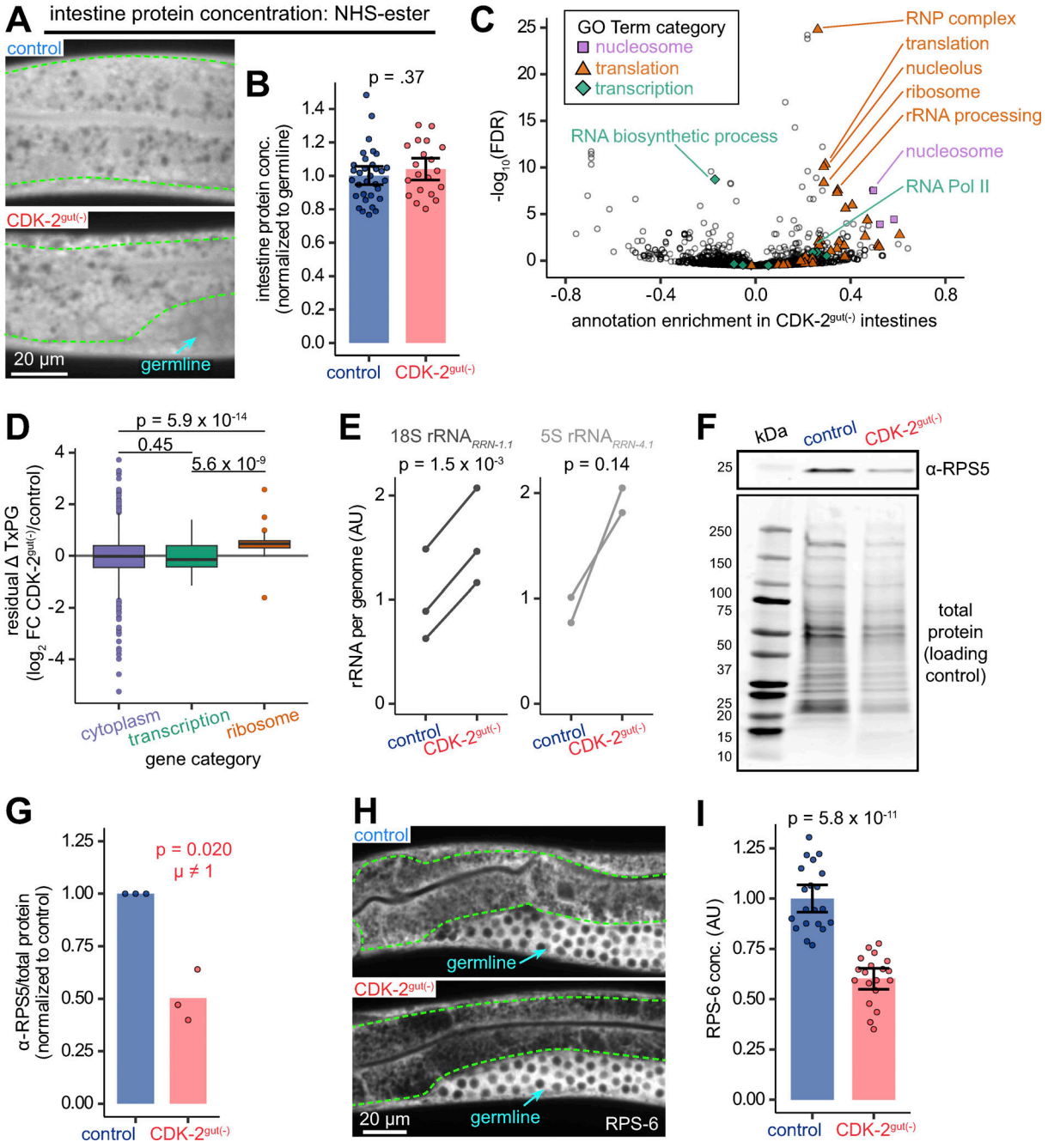

Figure 4. **Ribosome production increases when DNA content is limited. (A)** Confocal images of NHS-ester stain representing total protein in int2–int3 intestine rings of control and CDK-2$^{gut(-)}$ worms. **(B)** Quantification of cytoplasmic protein concentration in int2–int4 intestine rings from images as in A. **(C)** Volcano plot of GO terms for enrichment scores of transcripts in CDK-2$^{gut(-)}$ intestines compared with control. Colored GO terms are related to the nucleosome (lavender squares), translation (orange circles), or transcription (green diamonds). **(D)** Box plots of residual change in RNA abundance after accounting for expression level (TxPG in control, relationship visualized in Fig. 3 C). Log fold change in TxPG was regressed against expression level using a cubic polynomial. Groups are genes located in the cytoplasm (purple), involved in transcription (RNA Polymerase II subunit or general transcription factor; green) or ribosome subunits (orange). Kruskal–Wallis test P = 1.0 × 10^{-13}; P values shown are from post-hoc Dunn test with Benjamini-Hochberg multiple hypothesis testing correction. **(E)** Quantification of change in TxPG of the 18S or 5S rRNAs in control and CDK-2$^{gut(-)}$ intestines. Each connected pair of points represents one paired biological replicate. The mean TxPG of control is scaled to 1. P values are from paired *t* test with Benjamini-Hochberg multiple hypothesis testing correction. **(F)** Representative western blot showing total protein and anti-RPS-5 signal in dissected control and CDK-2$^{gut(-)}$ intestines. **(G)** Quantification of anti-RPS-5 signal normalized to total protein as in F, with control ratios for each blot scaled to 1. Each dot represents one experiment (*N* = 3 blots, *n* = 50–80 worms per genotype per blot). P value is of one sample *t* test against null hypothesis that μ = 1. **(H)** Confocal images of RPS-6::mCherry in int2–int4 intestine rings of control and CDK-2$^{gut(-)}$ worms. **(I)** Quantification of cytoplasmic RPS-6 concentration in int2–int4 intestine rings from images as in H. In B and I, each dot represents one worm, bars and error bars represent means and 95% confidence intervals, and P values are from Mann-Whitney U tests. Source data are available for this figure: SourceData F4.

(Fig. 4, F and G). Finally, we measured the amount of endogenously tagged RPS-6 (RPS-6::mCherry) in the intestine, showing that the concentration of RPS-6 in CDK-2$^{gut(-)}$ intestines was reduced to 60% of control (Fig. 4, H and I). The absolute reduction in rRNA and ribosomal protein abundance in CDK-2$^{gut(-)}$ intestines is reflective of a DNA-imposed limitation, but, like global mRNA, these ribosomal components are increased relative to DNA content.

Together, these data identify an additional layer of compensation where translational machinery is transcriptionally upregulated relative to other genes of a similar expression level, as mRNAs encoding ribosomal proteins increase their share of the intestine transcriptome from 2.2% of total mRNAs in control to 3.0% in CDK-2$^{gut(-)}$ intestines. However, this upregulation does not carry over to the protein level, where we observed decreased ribosome concentrations, and so this mechanism is insufficient to explain how global protein concentration is maintained in DNA-dilute cells. Recent work in vitro has shown that protein concentration can be maintained by increasing translation efficiency relative to protein degradation as cytoplasm becomes more dilute (Chen et al., 2024). Thus, we speculate that increased translation efficiency and decreased protein degradation rates likely buffer protein concentration in DNA-dilute cells.

DNA content is required for a major physiological role of the *C. elegans* intestine

In a highly biosynthetic organ like the intestine, we expect protein synthesis to be bottlenecked at the ribosome, and so the increase in production of some proteins in CDK-2$^{gut(-)}$ intestines, such as ribosomes themselves, may come at the expense of others. We, therefore, asked whether the intestinal function was compromised in CDK-2$^{gut(-)}$ worms. To test whether the DNA-dilute intestine could meet the nutritional demands of the worm, we measured the maximum body size and found that it was only slightly reduced in CDK-2$^{gut(-)}$ worms compared to control, and this difference was accounted for entirely by the reduced size of the intestine (Fig. 1 H; and Fig. 5, A and B). Worm development rate was also unaffected (Fig. 5 C), suggesting that DNA-dilute intestines are still able to meet the demands of organismal growth. This result contrasts with the observed correlation between nucleolus size and organism growth rate (Uppaluri et al., 2016), which may be due to the tissue specificity of our manipulation.

One of the main and most biosynthetically demanding functions of the intestine is to produce vitellogenin (VIT) yolk proteins. Thus, we explored the effect of reduced ploidy on the production of yolk protein and embryos. Analysis of our RNA-seq dataset revealed that yolk protein transcripts were only slightly compensated, in line with other highly expressed genes (Fig. 5 D), causing their share of the intestine transcriptome to decrease from 22% of total mRNAs in control to 15% in CDK-2$^{gut(-)}$ intestines. Unlike the compensation we saw for total protein, we found that CDK-2$^{gut(-)}$ animals produce substantially less yolk protein than their control siblings (Fig. 5, E and F), which we measured in the early embryos of their progeny. Notably, this decrease (13% of control) is far more severe than the decrease in VIT-2::GFP in embryos of worms where the binucleation is converted to an endoreduplication (van Rijnberk et al., 2022), which have ~85% of control VIT-2::GFP signal. The severity of this decrease in CDK-2$^{gut(-)}$ worms, especially compared to the reductions in either mRNA or ribosomes, suggests that worms actively shunt resources away from yolk production when DNA is limiting.

Consistent with phenotypes of mutations that reduce yolk protein levels, CDK-2$^{gut(-)}$ worms laid fewer eggs, and their progeny suffered developmental delays (Fig. 5, C and G). While CDK-2$^{gut(-)}$ worms from control mothers (CDK-2$^{gut(-)}$ F1s) developed at a normal rate, their progeny (CDK-2$^{gut(-)}$ F2s) developed more slowly despite having similar intestinal ploidy as F1s (Fig. 1, F and G), suggesting that this slow growth phenotype stems from defects in yolk deposition into the embryos that gave rise to these worms. These data indicate that ploidy reduction in the intestine severely impacts the specialized biosynthetic output of this tissue that supports progeny, constituting a severe fitness penalty to limiting DNA content.

One of the main advantages of our multicellular model is that we can study the consequences of diluting DNA in a terminally differentiated cell, which is not optimized to divide as rapidly as possible, unlike the proliferating cells in which DNA dilution has mostly been studied. We found that reduced polyploidy in the *C. elegans* intestine results in RNA dilution and a partially compensatory increase in the production capacity of each genome, and that other, unidentified, molecular mechanisms stabilize protein concentrations (Fig. 5 H). Importantly, these compensation mechanisms operate independently of the "sizer" mechanism which maintains molecular homeostasis by coupling cell size to DNA content in proliferating cells (Schmoller et al., 2015; Xie and Skotheim, 2020), and are thus compatible with terminal differentiation. Notably, we observed a twofold increase in mRNA and rRNA per genome, similar to what might be required to compensate for growth-mediated genome dilution over the course of a normal mitotic cell cycle. It is possible that yolk production is sacrificed to lessen the burden on translational machinery to maintain protein concentration and fulfill functions essential for organismal viability (Fig. 5 I).

Why would a tissue contain a few big cells instead of many small cells?

Our results show that limiting DNA content restricts the biosynthetic capacity of the *C. elegans* intestine with profound physiological effects, suggesting that this tissue requires a minimum amount of DNA to properly function. Why might polyploidy have evolved in this context as a strategy to increase DNA content as opposed to increasing the number of diploid cells? One explanation may be that increasing cell number during tissue development compromises tissue function. For example, increasing intestinal cell number during *C. elegans* embryogenesis can cause aberrant junction and apical surface formation, leading to lumen discontinuities and starvation (Sallee et al., 2021; Naturale et al., 2023; Demouchy et al., 2024). Cell division has also been shown to be an assault on embryonic intestine integrity as mitosis breaks existing cell–cell junctions (Sallee et al., 2021), and this problem is likely compounded in the larval intestine where structures are more mature, making animals prone to infection as the intestine is actively passing food.

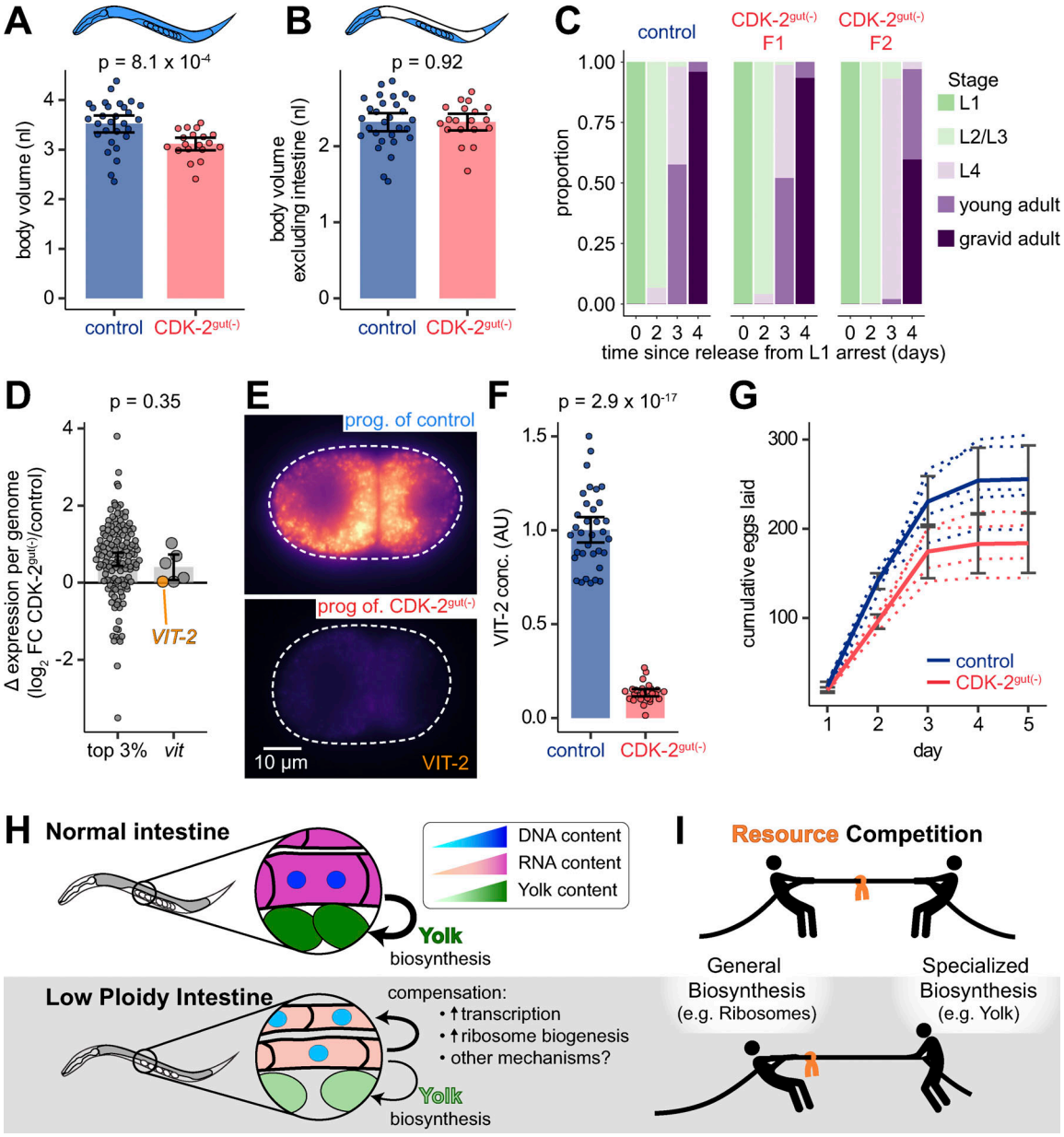

Figure 5. **Polyploidy in the intestine is essential for biological fitness. (A and B)** Quantification of body volume (A), and body volume excluding intestine (B) in control and CDK-2$^{gut(-)}$ worms. Each dot represents one worm. Volumes were estimated from length and cross-sectional area from images as in Fig. 1 H. **(C)** Developmental progression rate of tag-control, CDK-2$^{gut(-)}$ F1, and CDK-2$^{gut(-)}$ F2 animals. Stacked bar graphs show the average proportion of worms at the indicated developmental stage each day after release from overnight L1 arrest, grown at 15°C (N = 2 trials, n = 32–50 worms per genotype per trial). **(D)** Log_2 fold change in TxPG of either the top 3% most highly expressed transcripts or the six vitellogenin transcripts. Each dot represents one gene. **(E)** Representative widefield epifluorescence images of endogenously tagged VIT-2::GFP (viridis-inferno coloring) in F1 progeny of control and CDK-2$^{gut(-)}$ siblings. **(F)** Quantification of average VIT-2::GFP intensity in cytoplasm of one- to four-cell-stage embryos as in E. Each dot represents one embryo. In A, B, D, and F, bars and error bars represent means and 95% confidence intervals; P values are from Mann–Whitney U tests. **(G)** Cumulative number of eggs laid per day of adulthood in control and CDK-2$^{gut(-)}$ animals. Dotted lines show individual trails, solid lines represent the means, and error bars represent 95% confidence intervals. **(H)** Cartoon summarizing the cellular and organismal phenotypes of CDK-2$^{gut(-)}$ worms. **(I)** Cartoon depicting a hypothesized biosynthetic tradeoff between supporting the cell through general biosynthesis and supporting progeny through yolk production.

The human placenta contacts the uterus with a single, giant polyploid syncytium, and this continuous cell membrane is hypothesized to help resist invasion by maternal immune cells and pathogens that exploit cell junctions to breach epithelia (Zeldovich et al., 2013). In the *Arabidopsis* sepal, increased cell size due to polyploidy sets the critical curvature of the leaves protecting the developing bud (Roeder et al., 2012). This curvature may be dependent on mechanical properties due to the amount of cell wall, which is minimized when cells are large. Thus, somatic polyploidy may be an adaptive strategy to increase cell size in systems that are intolerant to abundant cell–cell contacts and future studies should test this model directly.

Materials and methods

Experimental model details

C. elegans and *P. pacificus* were grown on standard NGM plates seeded with OP50 *E. coli* at 20°C unless otherwise noted, according to standard laboratory practices (http://www.wormbook.org). The C terminus of the endogenous CDK-2 locus was edited using the SEC method using the guide sequence, 5′-ACCGCTGCTGAACAATCATC-3′ (Dickinson et al., 2015). Single-copy transgenes were generated with the RMCE method (Nonet, 2020). The extrachromosomal array was isolated in the F2 generation after microinjection. All other strains were generated by genetic crosses. Tables S1, S2, and S3 contain specific details of strain genotypes, allele descriptions, and plasmids used to generate strains. The specific strains used in each experiment are detailed in Table S1.

Microscopy equipment

Images used to measure ploidy, nucleus and nucleolus volume, cell size (GFP::CAAX), and AMA-1, FIB-1, and RPS-6 abundance were acquired using a Zeiss Axio Observer Microscope (Carl Zeiss) with a PlanApoChromat 40×/1.3NA objective, Prime BSI Express sCMOS camera (Photometrics), and CSU-W1 spinning disk (Yokogawa), controlled using Slidebook software (Intelligent Imaging Innovations). Referred to as the "Zeiss spinning disk" below.

Images used to measure mRNA, protein, and NLS-mScarlet concentration were acquired using a Nikon Ti-E inverted microscope (Nikon Instruments) with a PlanApoChromat 40×/1.3NA objective, a Yokogawa CSU-X1 confocal spinning disk head, and an Andor Ixon Ultra back thinned EM-CCD camera (Oxford Instruments - Andor), controlled by NIS Elements (Nikon Instruments), referred to as the "Nikon spinning disk" below.

Images used to measure body and intestine volume and VIT-2 concentration were acquired using a Nikon Eclipse Ni upright microscope (Nikon Instruments) with a 10×/0.25NA or 40×/1.3NA objective, Lumencore Sola Light Engine, and an Andor Zyla DG-152V-C1E-F1 5.5 Megapixel Front illuminated Scientific CMOS camera (Oxford Instruments – Andor), controlled by NIS Elements (Nikon Instruments), referred to as the "Nikon widefield" below.

Counting intestinal nuclei

Fluorescent nuclei (histone::mCherry) were counted on our Nikon widefield microscope at the L1 stage to determine cell number and at the L4 stage to determine the final nucleus number. Live worms were imaged on 3% agarose pads and immobilized with 2 mM Levamisole.

Analysis of intestinal tissue

We chose to focus on cells in the anterior intestine for most experiments (including ploidy, total mRNA, total protein quantification, RNA-seq, and abundance of Pol II, NLS-mScarlet, FIB-1, and ribosomal proteins and RNAs) to make our quantification and imaging consistent across worms. It was not feasible to consider the whole intestine in experiments requiring either image analysis or dissection: in images of intact worms, the intestine is not usually contained on a flat plane, meaning that the more posterior int rings are contained within different Z planes than the more anterior cells. Therefore, we restricted the analysis of images to int2–int4 for practical reasons: these rings are close to a neighboring tissue, the pharynx, that was marked with fluorescence to distinguish genotypes (Fig. 1 C), close to the germline for normalization, and frequently positioned toward the coverslip in the same (or nearly the same) plane as the germline, also helping to standardize our normalization. Ploidy measurements included int1. The RNA-seq was performed in dissected anterior halves of intestines, approximately int2–int4, as we wanted to collect the sample rapidly to avoid RNA degradation, and so elected to discard the posterior intestine because it was often hard to fully remove both halves of the intestine from the body cavity. In contrast, Pol II ChIP-seq experiments likely enriched for Pol II-nanobody complexes throughout the intestine.

Representative images

In experiments involving tissue staining, we observed significant variation in fluorescence intensity between worms (even control worms), likely due to staining variability. To account for this variation and facilitate direct visual comparison between samples, we normalized the fluorescence intensity of the intestine to that of the germline within the same animal. Displayed images are scaled so that the intensities of the germlines appear similar between genotypes since the meaningful comparison is between the intestine and germline of the same worm. Representative images were chosen that had an intestine/germline fluorescence intensity ratio similar to the mean of that genotype (see Fig. 1 F, Fig. 2 A, and Fig. 4 A). Representative images from live worms were scaled identically for display.

Ploidy quantification and estimation of total organ ploidy

Day 1 adult *C. elegans* were washed in M9 for 20 min to remove bacteria. Worms were permeabilized in PBS + 0.1% Tween 20 (PBST) + 0.1% Triton X-100 for 10 min, washed 2x in PBST, and fixed overnight in freshly prepared Carnoy's solution (60% ethanol, 30% chloroform, and 10% glacial acetic acid) at 4°C. Worms were rehydrated with 5 min washes at 4°C in 70% ethanol, 30% ethanol in 1X PBS, and 1X PBS. Worms were stained with 500 ng/µl Hoescht 33342 for 1 h at 37°C in PBST, washed 3x for 10 min at room temperature in PBST, and mounted in VectaShield. Worms were imaged with our Zeiss spinning disk microscope with a 0.3 or 0.6 µm z-step. We found no difference in ploidy quantification between the narrow or wide z-step, so measurements from both experiments were combined. We excluded images of worms whose intestines were not oriented toward the coverslip.

Nuclei were segmented using StarDist (Weigert et al., 2020) software followed by manual correction. Crops of images of both low ploidy and control intestines were manually segmented using Napari software to create ground truth training data. Images and labels were upscaled 2× or 4× in z to make nuclei more isometric for 0.3 and 0.6 µm z-step images, respectively, and then a 3D StarDist model was trained using default parameters. StarDist predictions were downscaled to z to generate

labels with original dimensions. These labels were manually corrected, intestine and pachytene germline nuclei were identified, and the sum intensity of each nucleus was calculated using a custom Python script with Napari and Napari-Simpleitk-image-processing packages. The cytoplasmic background was obtained manually from unstained images. C values (ploidy) were obtained using a custom R script: cytoplasmic background was subtracted from nucleus intensity values, and then corrected intensity values of intestinal nuclei were normalized to those of tetraploid pachytene germline nuclei (C = 4).

Total intestine ploidy was calculated as average nucleus number (N_{nuc}) × average nucleus ploidy (C_{nuc}). Intestine DNA concentration was calculated as total intestine ploidy (C_{tot})/average intestine volume (nl). The error of these measurements was combined as

$$\left[\frac{error(C_{tot}/nl)}{C_{tot}/nl}\right]^2 = \left[\frac{sd(C_{nuc})}{C_{nuc}}\right]^2 + \left[\frac{sd(nl)}{nl}\right]^2 + \left[\frac{sd(N_{nuc})}{N_{nuc}}\right]^2.$$

Measurement of body and cell size

To measure maximum body and intestine size, day 2 adults (96 h post egg lay) were imaged in bright field on our Nikon widefield microscope at 10×. The body and intestine were outlined in FIJI, and the area and length were measured. Volume was estimated as a cylinder: V = π × (0.5 × area/length)^2 × length since the area is measured in the anterior–posterior × dorsal–ventral plane. Average cell size was estimated as intestine volume/20 since cell number is unchanged between genotypes (Fig. 1 D).

To corroborate our measurement of cell width, which is more sensitive to error than organ length, we measured the width of cells expressing the intestine-specific membrane reporter, *elt-2p::GFP::CAAX*, as an extrachromosomal array. Day 2 adults were imaged on our Zeiss spinning disk microscope at 40× and with a 0.3 µm z-step. Lines were drawn in FIJI from the apical to the basal surface of each cell, perpendicular to the lumen of the intestine, and at the midpoint of the cell volume in z, and the width was measured. Cells that were twisted or diagonal in z were ignored. For our statistical test, cell position was included in the linear model because of the clear decrease in cell width from anterior to posterior.

Live imaging experiments for AMA-1 and FIB-1 amount and volume (organelle size), NLS-mScarlet transgene abundance, and RPS-6 concentration

Age-synchronized (72 h post egg lay) worms expressing endogenously tagged AMA-1::GFP or RPS-6::mCherry, or endogenous wrmScarlet11::FIB-1 and an *eft-3p::wrmScarlet1-10* transgene were imaged on our Zeiss spinning disk microscope at 40× and with a 0.3 µm z-step. Age-synchronized (96 h post egg lay) worms expressing an *asp-1p::2x-nls-mScarlet* single copy transgene were imaged on our Nikon spinning disk microscope at 40× and with a 0.3 µm z-step. All live worms were imaged on 3% agarose pads and immobilized with 2 mM Levamisole. To avoid confounding effects of losing signal with imaging at increased depth in the tissue, we identified a focal plane of the hypodermal cell nuclei closest to the coverslip and imaged 12–15 µm into the tissue, excluding images of worms whose intestines were not oriented toward the coverslip. Images were segmented manually (AMA-1 or NLS-mScarlet: nuclei, FIB-1: nucleoli, and RPS-6: cytoplasm excluding nuclei and large gut granules), and organelle volume and average fluorescence intensities were calculated using the Napari-Simpleitk-image-processing package. The background was measured from the cytoplasmic signal for nuclear proteins or from wild-type worms for cytoplasmic RPS-6. The background was subtracted from mean fluorescence intensity values, and the total fluorescence intensity was calculated as background-corrected mean × volume. For nucleus volume and AMA-1 total intensity measurements in binucleate cells, values from the two nuclei were summed to give a metric of the total volume of nuclei and total Pol II within a cell. Due to the variability in binucleation in CDK-2$^{gut(-)}$ intestinal cells, we report the total nuclear volume and AMA-1 intensity, per cell. 95% confidence intervals were calculated via bootstrap using the smean.cl.boot function in the R Hmisc package. Data were plotted in R.

Total mRNA/poly(A)-FISH sample preparation and imaging

The fluorescence in situ hybridization protocol was adapted from Lee et al. (2017). Worms were age-standardized by egg lay and fixed 72 h later. Worms were fixed for 35 min in PBST + 4% formaldehyde, washed 1x in PBST, the cuticle was permeabilized in PBST + 0.1% Triton X-100 for 10 min, washed 2x in PBST, and then permeabilized overnight at 4°C in 70% ethanol. On day 2, fixed worms were washed 1x in FISH wash buffer (FISHw, 2x SSC + 10% formamide + 0.1% Tween 20), then incubated overnight at 37°C in FISH hybridization buffer (Biosearch) + 10% formamide + 833 nM T30-Califluor 590 oligo (Biosearch). On day 3, worms were washed 1x in FISHw, incubated 30 min at 37°C in FISHw + 1 µM Hoescht 33342, washed 2x in FISHw, and mounted in VectaShield. Slides were imaged on our Nikon spinning disk microscope. To avoid confounding effects of losing signal with imaging at increased depth in the tissue, we identified a focal plane of the hypodermal cell nuclei closest to the coverslip and imaged 10.8 µm into the tissue, excluding images of worms whose intestines were not oriented toward the coverslip.

Total protein sample preparation and imaging

Worms were age-synchronized, fixed, and permeabilized as described above for poly(A)-FISH, above. Fixed worms were washed 1x in 0.1 M sodium bicarbonate, pH 8.3 + 0.1% Tween 20 (SBT), incubated for 1 h at 37°C in SBT + 1 µM Hoescht 33342 + 5 µg/ml NHS-ester-A647 (Invitrogen), washed 3x SBT, and mounted in VectaShield. Slides were imaged and included in the analysis as described for the poly(A)-FISH experiment, above.

Poly(A)-FISH and total protein image analysis and quantification

We discarded images of worms whose intestines were not oriented toward the coverslip. We manually segmented the nucleus and cell (and nucleolus for poly(A)-FISH) for each visible nucleus within the int2–int4 rings. Only the focal plane where each nucleus was largest was used for measurement. Representative images in Figs. 2 and 4 show crops to int2–int3. Several planes of

the pachytene germline or proximal oocytes were also labeled for within-worm normalization because absolute intensity values were highly variable between worms due to staining variability. New segmentations were calculated for the cytoplasm (cell–nucleus) and nucleoplasm (nucleus–nucleolus). The background was estimated from unstained worms for poly(A)-FISH and from the slide for total protein. To calculate cytoplasmic intensity, background-subtracted intensities for each label were normalized to the germline signal in each worm. The mean of all cytoplasmic measurements was calculated for each worm and then scaled so that the mean of the control means was 1. To calculate the nucleoplasmic/cytoplasmic mRNA ratio, the nucleoplasm/cytoplasm ratio was calculated for each nucleus, then averaged for each worm, and then scaled such that the mean of controls was 1. Images were segmented and measured using a custom Python script with Napari and Simpleitk packages. 95% confidence intervals were calculated via bootstrap using the smean.cl.boot function in the R Hmisc package. Data were plotted in R.

Spike-in normalized RNA-seq sample preparation

P. pacificus transcripts can be easily distinguished from those of *C. elegans*, but the tissue is expected to behave similarly at each step of sample processing. Three independent biological replicates were performed. DNA and RNA were extracted from dissected intestines. Day 1 adult *C. elegans* (72 h post egg lay) and *P. pacificus* (96 h post egg lay) were dissected and immediately flash frozen in liquid nitrogen. To dissect, worms were picked into drops of 340 mOsm L-15/FBS media (Fernandes Póvoa et al., 2020) with 3 mM Levamisole to paralyze on a slide covered with Scotch tape. Working in batches, worms were cut behind the pharynx with a 25-gauge needle, then the intestine was cut away from the body. Intestines were washed 1x in L-15/FBS media to remove traces of other tissues, then transferred to PCR tubes, and flash-frozen in liquid nitrogen. Tissue was thawed directly into Trizol and lysates from each genotype were combined. An equal amount of *P. pacificus* lysate was distributed between tag control and CDK-2$^{gut(-)}$ F1 lysates (N = 3 experiments, $n \approx 40$ *P. pacificus* and either 80 control or 240 CDK-2$^{gut(-)}$ F1 intestines per sample). Samples were split to separately extract RNA and DNA: RNA was extracted using Zymo Direct-zol Microprep kit, and DNA was extracted using Zymo DNA-quick microprep plus with a 4:1 DNA binding buffer:lysate ratio. RNA quality was assessed on a BioAnalyzer (RIN range from 8.7 to 10). RNA-seq libraries were prepared using NEBNext Single Cell/Low Input RNA Library Prep Kit for Illumina (NEB). Pooled libraries were sequenced with paired-end sequencing on a Novoseq 6000 by Novogene.

rRNA and DNA measurements

DNA and rRNA amounts were quantified by qPCR from the spike-in normalized DNA and RNA samples described above. For rRNA quantification, cDNA was synthesized using the Superscript IV kit and random hexamers. qPCR was performed in technical triplicate using the PowerTrack SYBR Master Mix kit with primers against the *C. elegans* 18S and 5S rRNAs (*rrn-1.1* and *rrn-4.1*, respectively) and the *P. pacificus* 18S rRNA (*Ppa-rrn-1.1*). qPCR was performed similarly for DNA quantification using primers against a repetitive region of the *C. elegans* genome and the rDNA of *P. pacificus* (*Ppa-rrn-1.1*). Oligo sequences are listed in Table S4. RNase and DNase treatments of DNA and RNA samples, respectively, ensured that rRNA and rDNA did not erroneously contribute to the quantification of the other. Standard curves were made using these primers using DNA and RNA templates prepared similarly to above and confirmed that these primers uniquely amplified targets from each species. For each sample, a DNA normalization factor was calculated from the DNA Cq values as $2^{-\Delta Cq_{(Cel-Ppa)}}$, which reflects the ratio of *C. elegans* to *P. pacificus* DNA. For each rRNA, the rRNA per genome was calculated from the RNA Cq values and DNA normalization factor as $\frac{2^{-\Delta Cq_{(Cel-Ppa)}}}{DNA\ norm.\ factor}$.

RNA-seq analysis

Fragments were aligned to concatenated WS284 *C. elegans* and *P. pacificus* genomes using a STAR aligner with default parameters. Aligned reads were counted for each gene with featureCounts in R without multimappers. Counts were converted to transcripts per million (TPM) with the countToFPKM package in R. Transcripts per genome (TxPG) for each gene were then calculated by multiplying the TPM by a sample normalization factor:

$$TxPG = TPM \times \frac{\sum TPM_{Cel} / \sum TPM_{Ppa}}{DNA\ norm.\ factor}.$$

Within each genotype, we calculated the geometric mean of TxPG values for each gene, excluding genes with TxPG = 0 in any sample, and then calculated the CDK-2$^{gut(-)}$-to-CDK-2::ZF::GFP tag control ratio of the geometric means. We report the $\log_2$ of these fold changes. Genes were excluded from analysis if they had few reads across samples (DESeq2 baseMean < 10) or were not expressed in the intestine. Genes were categorized as being expressed in the intestine if they had $TxPG_{control} > 2$ or were identified as expressed in the intestine by Kaletsky et al. (2018). Results from this analysis are available in Table S5.

We quantified the trend in Fig. 3 C through a polynomial regression with four terms ($y \sim ax^0 + bx^1 + cx^2 + dx^3$) in R. To test if this trend was caused by aberrant expression of stress response or cell cycle genes, we repeated that analysis after excluding genes with either GO biological process (GOBP) term "response to stress" or "cell cycle." We further analyzed the enrichment of GO terms using the 1D enrichment function in Perseus software (Cox and Mann 2012). We included all GO terms and keywords for the enrichment analysis and hypothesis testing but limited our further analysis to GOBP and GO cellular compartment (GOCC) terms, which were the most interpretable. Results from this analysis are available in Table S6. Genes were included in Fig. 4 D if they were directly annotated with GO terms listed in Table S8, and we report the residual $\log_2$ fold change of the regression described above.

The fraction of the transcriptome comprised of vitellogenin transcripts was calculated from the unadjusted TPMs in each sample as: $\sum TPM_{VIT} / \sum TPM_{non-VIT, \int -expressed}$. The geometric mean of these fractions was reported for each genotype. An analogous calculation was made for the fraction of the transcriptome comprised of ribosomal protein subunit transcripts.

ChIP-seq sample preparation

Four tag control and three CDK-2$^{gut(-)}$ biological replicates were performed. For each replicate, 450,000 (control) or 600,000 (CDK-2$^{gut(-)}$) age-synchronized adult worms were flash-frozen in liquid nitrogen. To synchronize, we picked several L4, balancer-negative worms (P0, JLF1584 control or JLF1585 CDK-2$^{gut(-)}$) to NGM plates. Worms were grown at 15°C to aid in monitoring of growth rate. Populations were allowed to starve, then starved F2 L1s were plated onto new 15 cm NGM peptone-rich plates seeded with NA22 *E. coli* (XL plates) at 30,000 (control) or 45,000 (CDK-2$^{gut(-)}$) worms per plate. Gravid adults were bleached until most worms burst open (6–7.5 min vortexing at room temperature in a solution of 2% sodium hypochlorite + 300 mM KOH), washed 4x in M9, resuspended in egg buffer, filtered through a sterile, 40-µm cell strainer, and hatched overnight at room temperature. Newly synchronized F3 L1s were again plated on XL plates and allowed to grow until adulthood when they were washed in cold M9, resuspended in PBS with protease inhibitors (PI; 2X Halt Protease Inhibitor Cocktail + 2 mM PMSF), and dripped into liquid nitrogen to form worm "Dippin-dots." Frozen worms were ground with a mortar and pestle and cooled with liquid nitrogen.

Our ChIP protocol was based on the protocol by Sen et al. (2021), in which buffer compositions and recipes can be found. Worm powder was thawed directly into PBS + PI + 1.1% formaldehyde and crosslinked for 7 min at room temperature. Working on ice from this point, each sample was pelleted, resuspended in B-ChIP-L0 to a final volume of 1.6 ml, and divided between four screw cap tubes. 0.8 ml ceramic beads were added to each tube and worm pieces were lysed with a Fast Prep (three cycles of 30 s at 5.5 M/s). Lysate was combined into two microcentrifuge tubes, brought up to 1.2 ml volume with B-ChIP-L0, and sonicated with a Branson 250 Sonifier. Lysates were cleared by centrifuging 2 × 5 min at 20,000 *g*. Affinity resin was prepared at room temperature: 100 µl Protein G Dynabeads (Invitrogen) was washed 3x in B-ChIP-BL (0.5 mg/ml BSA in PBS), blocked in B-ChIP-BL for 40 min, bound to 19 µg anti-V5 antibody (SV5-Pk1; Bio-Rad), and washed 3x with B-ChIP-BL. Affinity resin was incubated overnight at 4°C with the cleared lysate, then washed 2x with low salt wash buffer, 1x with high salt wash buffer, 2x with LiCl-containing wash buffer, and 2x in TE + 50 mM NaCl. On a ThermoMixer (Eppendorf) at 800 rpm, chromatin was eluted in B-ChIP-EL for 15 min at 65°C, then treated with 0.4 mg/ml RNase A for 1 h at 37°C followed by 0.4 mg/ml proteinase K for 2 h at 55°C, and, finally, crosslinks were reversed overnight at 65°C. DNA was cleaned using the ChIP DNA Clean & Concentrator (ZYMO). Libraries were prepared using NEBNext Ultra II DNA Library Prep Kit for Illumina (NEB). Libraries were pooled and sequenced with paired-end sequencing on a Novoseq 6000 by Novogene.

ChIP-seq analysis

Fragments were aligned to the WBPS18 *C. elegans* genome using bowtie2. We generated meta-gene occupancy profiles surrounding the transcription start site (TSS) for each gene using the genomation package in R. For analyses involving Pol II occupancy at the TSS, we defined the TSS to be 100 bp upstream to 200 bp downstream of the annotated TSS for each gene based off of these profiles (Fig. S2 I). We calculated the coverage of the 50-bp mid-point of each uniquely mapped fragment (i.e., midpoint ± 25 bp) of all gene bodies and TSSs using custom-written Python scripts, calculating both counts (gene bodies and TSS) and fragments per kilobase million (FPKM, gene bodies only) for each gene. Samples were excluded if the distribution of FPKM values was not highly bimodal, which indicated poor enrichment of intestine-specific gene bodies during the pull-down. The geometric mean of FPKM values (gene bodies) or counts (TSSs) was calculated across control samples for each gene, referred to as occupancy in control. Differential occupancy was calculated from the count data using DESeq2 for both genes and TSSs. Genes were excluded from analysis if they had few reads across samples (DESeq2 baseMean < 10) or were not highly occupied in the intestine. Genes were categorized as being expressed in the intestine if they were identified as expressed in the intestine by Kaletsky et al. (2018) or had either baseMean or control FPKM values greater than the average of genes not expressed in the intestine in our RNA-seq experiment. The fold change from DESeq2 was then plotted against either the expression level in control, calculated from our RNA-seq data, or the occupancy in control. Similar results were seen using either occupancy quantifications from TSSs or gene bodies. Results from these analyses are available in Table S7. We note that some of the differences between our RNA-seq and ChIP-seq experiments may also be due to the contribution of the posterior intestine or the use of CDK-2$^{gut(-)}$ F3 worms in the ChIP experiment, whereas the RNA-seq experiment only used anterior intestines and CDK-2$^{gut(-)}$ F1 worms.

Estimation of ribosome concentration via western blot

Anterior intestines from day 2 adult worms were dissected into egg buffer and flash-frozen in liquid nitrogen. Intestines were thawed into 1x Laemmli sample buffer (Bio-Rad), pooled (40 for control, 80 for CDK-2$^{gut(-)}$), and incubated for 10 min at 95°C. Lysates were loaded onto a 4–15% SDS polyacrylamide gel (Bio-Rad) and run for 1 h at 120 V. Protein was transferred to a nitrocellulose membrane overnight in Towbin's transfer buffer at 25 V on ice. Membranes were stained with REVERT total protein stain (LI-COR) and imaged in the 700-nm channel on an Odyssey DLx Imager (LI-COR). Membranes were blocked in 5% non-fat, dry milk in PBST, then stained with mouse 1:200 anti-RPS5-Alexa Fluor 546 (1°; sc-390935-A546; Santa Cruz Biotechnology; Nousch, 2020) followed by 1:10,000 IRDye 800CW goat anti-mouse IgG (2°, 926–32210; LI-COR). The A546 fluor was not used for quantification. Membranes were imaged again for the 800 nm channel. Images were processed in FIJI. The background was subtracted and the total RPS-5 signal was divided by the total protein signal for each lane as a metric for the ribosome fraction of the proteome. Since there is, by definition, no variation in the control RPS-5/total protein, we performed a one sample *t* test on CDK-2$^{gut(-)}$ ratios against the null hypothesis that mean (µ) = 1.

Vitellogenin concentration

Age-synchronized, gravid adults (72 h after egg lay) were picked into a 30-µl drop of M9 on a coverslip, then immobilized by

placing the slide on a T-75 cell culture flask filled with ice water, and then cut with a No. 10 scalpel to release eggs. Eggs in M9 were mixed 1:1 with 60% Iodixanol (OptiPrep; Sigma-Aldrich) to better match the refractive index of the egg (Xiong and Sugioka, 2020). Coverslips were inverted onto slides and sealed with petroleum jelly. One to four cell-stage embryos were imaged with our Nikon widefield using a 60×/NA1.4 objective in the focal plane where the nuclei were the largest.

Brood size

L4 worms (48 h post egg lay) were picked to individual, lightly seeded NGM plates (50 µl stationary phase OP50 grown for 6 h). Each day after, adults were transferred to new plates and the embryos were counted.

Growth rate

Worms were grown at 15°C. Gravid adults (P0) were bleached in 10 µl of bleach solution (2% sodium hypochlorite + 0.5 M KOH) on unseeded NGM plates. The next day, arrested F1 L1s were transferred to new, seeded plates. Every day after, we counted the number of worms in each developmental stage and transferred L4s to new plates to avoid confusing the F2 progeny of fast-growing F1s with slow-growing F1s.

Online supplemental material

Figs. S1, S2, and S3 contain additional data related to ploidy quantification and organ and cell size (Fig. S1), RNA- and ChIP-seq (Fig. S2), and NLS-mScarlet and FIB-1 abundance (Fig. S3). Table S1 details specific nematode strains and genotypes used in each experiment. Table S2 details genetic alleles used in this study. Table S3 details plasmids used in this study. Table S4 details oligos used in this study. Table S5 contains calculated values from the RNA-seq experiment. Table S6 contains GO term 1D enrichment scores from the RNA-seq experiment. Table S7 contains calculated values from the ChIP-seq experiment. Table S8 contains GO terms that were used in this study and associated gene names.

Data availability

Raw sequencing data and intermediate analyses are available at GEO at GSE280911 (RNA-seq) and GSE280912 (ChIP-seq). The 3D StarDist model used for segmenting *C. elegans* nuclei and code for calculating ploidy and analyzing RNA- and ChIP-seq data are available at https://github.com/atlessenger/lessenger_2024_jcb. All other codes, reagents, and raw data are available upon request.

Acknowledgments

We thank Georgi Marinov for sharing of code and Alex Long and Tim Stearns for the use of their confocal microscope. We thank Dominique Bergman, Lucy O'Brien, Lauren Cote, Andrew Fire, Hannah Fung, Kang Shen, Shicong Xie, and members of the Feldman and Skotheim labs for scientific discussions and feedback, and for their comments on the manuscript.

This work was supported by Cell and Molecular Biology Training Grant T32 GM007276 and a Stanford Graduate Fellowship awarded to A.T. Lessenger, a National Institutes of Health New Innovator Award DP2 GM119136-01 and RO1 GM133950 and 1R35GM153310 awarded to J.L. Feldman, and GM134858 awarded to J.M. Skotheim. Some strains were provided by CGC and funded by the NIH Office of Research Infrastructure Programs (P40 OD010440).

Author contributions: A.T. Lessenger: Conceptualization, Formal analysis, Funding acquisition, Investigation, Methodology, Software, Visualization, Writing - original draft, Writing - review & editing, J.M. Skotheim: Conceptualization, Project administration, Resources, Supervision, M.P. Swaffer: Methodology, Supervision, Writing - review & editing, J.L. Feldman: Conceptualization, Funding acquisition, Methodology, Project administration, Supervision, Visualization, Writing - original draft, Writing - review & editing.

Disclosures: The authors declare no competing interests exist.

Submitted: 26 March 2024
Revised: 27 September 2024
Accepted: 19 November 2024

References

Armenti, S.T., L.L. Lohmer, D.R. Sherwood, and J. Nance. 2014. Repurposing an endogenous degradation system for rapid and targeted depletion of C. elegans proteins. *Development*. 141:4640–4647. https://doi.org/10.1242/dev.115048

Berry, S., M. Müller, A. Rai, and L. Pelkmans. 2022. Feedback from nuclear RNA on transcription promotes robust RNA concentration homeostasis in human cells. *Cell Syst*. 13:454–470.e15. https://doi.org/10.1016/j.cels.2022.04.005

Cantwell, H., and P. Nurse. 2019. Unravelling nuclear size control. *Curr. Genet*. 65:1281–1285. https://doi.org/10.1007/s00294-019-00999-3

Chen, Y., G. Zhao, J. Zahumensky, S. Honey, and B. Futcher. 2020. Differential scaling of gene expression with cell size may explain size control in budding yeast. *Mol. Cell*. 78:359–370.e6. https://doi.org/10.1016/j.molcel.2020.03.012

Chen, Y., J.-H. Huang, C. Phong, and J.E. Ferrell Jr. 2024. Viscosity-dependent control of protein synthesis and degradation. *Nat. Commun*. 15:2149. https://doi.org/10.1038/s41467-024-46447-w

Claude, K.-L., D. Bureik, D. Chatzitheodoridou, P. Adarska, A. Singh, and K.M. Schmoller. 2021. Transcription coordinates histone amounts and genome content. *Nat. Commun*. 12:4202. https://doi.org/10.1038/s41467-021-24451-8

Cox, J., and M. Mann. 2012. 1D and 2D annotation enrichment: A statistical method integrating quantitative proteomics with complementary high-throughput data. *BMC Bioinformatics*. 13:S12. https://doi.org/10.1186/1471-2105-13-S16-S12

Darmasaputra, G.S., L.M. van Rijnberk, and M. Galli. 2024. Functional consequences of somatic polyploidy in development. *Development*. 151:dev202392. https://doi.org/10.1242/dev.202392

Dej, K.J., and A.C. Spradling. 1999. The endocycle controls nurse cell polytene chromosome structure during Drosophila oogenesis. *Development*. 126:293–303. https://doi.org/10.1242/dev.126.2.293

Demouchy, F., O. Nicolle, G. Michaux, and A. Pacquelet. 2024. PAR-4/LKB1 prevents intestinal hyperplasia by restricting endoderm specification in Caenorhabditis elegans embryos. *Development*. 151:dev202205. https://doi.org/10.1242/dev.202205

Dickinson, D.J., A.M. Pani, J.K. Heppert, C.D. Higgins, and B. Goldstein. 2015. Streamlined genome engineering with a self-excising drug selection cassette. *Genetics*. 200:1035–1049. https://doi.org/10.1534/genetics.115.178335

Edgar, B.A., N. Zielke, and C. Gutierrez. 2014. Endocycles: A recurrent evolutionary innovation for post-mitotic cell growth. *Nat. Rev. Mol. Cell Biol*. 15:197–210. https://doi.org/10.1038/nrm3756

Fernandes Póvoa, E.E., A.L.P. Ebbing, M.C. Betist, C. van der Veen, and H.C. Korswagen. 2020. An optimized dissociation protocol for FACS-based

isolation of rare cell types from *Caenorhabditis elegans* L1 larvae. *MethodsX*. 7:100922. https://doi.org/10.1016/j.mex.2020.100922

Frank, D.J., and M.B. Roth. 1998. ncl-1 is required for the regulation of cell size and ribosomal RNA synthesis in Caenorhabditis elegans. *J. Cell Biol.* 140: 1321–1329. https://doi.org/10.1083/jcb.140.6.1321

Gentric, G., and C. Desdouets. 2014. Polyploidization in liver tissue. *Am. J. Pathol.* 184:322–331. https://doi.org/10.1016/j.ajpath.2013.06.035

Hansson, K.-A., E. Eftestøl, J.C. Bruusgaard, I. Juvkam, A.W. Cramer, A. Malthe-Sørenssen, D.P. Millay, and K. Gundersen. 2020. Myonuclear content regulates cell size with similar scaling properties in mice and humans. *Nat. Commun.* 11:6288. https://doi.org/10.1038/s41467-020-20057-8

Hedgecock, E.M., and J.G. White. 1985. Polyploid tissues in the nematode Caenorhabditis elegans. *Dev. Biol.* 107:128–133. https://doi.org/10.1016/0012-1606(85)90381-1

Kaletsky, R., V. Yao, A. Williams, A.M. Runnels, A. Tadych, S. Zhou, O.G. Troyanskaya, and C.T. Murphy. 2018. Transcriptome analysis of adult Caenorhabditis elegans cells reveals tissue-specific gene and isoform expression. *PLoS Genet.* 14:e1007559. https://doi.org/10.1371/journal.pgen.1007559

Lanz, M.C., E. Zatulovskiy, M.P. Swaffer, L. Zhang, I. Ilerten, S. Zhang, D.S. You, G. Marinov, P. McAlpine, J.E. Elias, and J.M. Skotheim. 2022. Increasing cell size remodels the proteome and promotes senescence. *Mol. Cell.* 82:3255–3269.e8. https://doi.org/10.1016/j.molcel.2022.07.017

Lee, L.-W., C.-C. Lee, C.-R. Huang, and S.J. Lo. 2012. The nucleolus of Caenorhabditis elegans. *J. Biomed. Biotechnol.* 2012:601274. https://doi.org/10.1155/2012/601274

Lee, C., H.S. Seidel, T.R. Lynch, E.B. Sorensen, S.L. Crittenden, and J. Kimble. 2017. Single-molecule RNA fluorescence in situ hybridization (smFISH) in *Caenorhabditis elegans*. *Bio Protoc.* 7:e2357. https://doi.org/10.21769/BioProtoc.2357

Ma, Y., K. Jonsson, B. Aryal, L. De Veylder, O. Hamant, and R.P. Bhalerao. 2022. Endoreplication mediates cell size control via mechanochemical signaling from cell wall. *Sci. Adv.* 8:eabq2047. https://doi.org/10.1126/sciadv.abq2047

Marshall, W.F., K.D. Young, M. Swaffer, E. Wood, P. Nurse, A. Kimura, J. Frankel, J. Wallingford, V. Walbot, X. Qu, and A.H. Roeder. 2012. What determines cell size? *BMC Biol.* 10:101. https://doi.org/10.1186/1741-7007-10-101

Metzl-Raz, E., M. Kafri, G. Yaakov, and N. Barkai. 2020. Gene transcription as a limiting factor in protein production and cell growth. *G3.* 10: 3229–3242. https://doi.org/10.1534/g3.120.401303

Mu, L., J.H. Kang, S. Olcum, K.R. Payer, N.L. Calistri, R.J. Kimmerling, S.R. Manalis, and T.P. Miettinen. 2020. Mass measurements during lymphocytic leukemia cell polyploidization decouple cell cycle- and cell size-dependent growth. *Proc. Natl. Acad. Sci. USA.* 117:15659–15665. https://doi.org/10.1073/pnas.1922197117

Naturale, V.F., M.A. Pickett, and J.L. Feldman. 2023. Persistent cell contacts enable E-cadherin/HMR-1- and PAR-3-based symmetry breaking within a developing C. elegans epithelium. *Dev. Cell.* 58:1830–1846.e12. https://doi.org/10.1016/j.devcel.2023.07.008

Neurohr, G.E., R.L. Terry, J. Lengefeld, M. Bonney, G.P. Brittingham, F. Moretto, T.P. Miettinen, L.P. Vaites, L.M. Soares, J.A. Paulo, et al. 2019. Excessive cell growth causes cytoplasm dilution and contributes to senescence. *Cell.* 176:1083–1097.e18. https://doi.org/10.1016/j.cell.2019.01.018

Nonet, M.L. 2020. Efficient transgenesis in *Caenorhabditis elegans* using flp recombinase-mediated cassette exchange. *Genetics.* 215:903–921. https://doi.org/10.1534/genetics.120.303388

Nousch, M. 2020. RPL-4 and RPL-9-Mediated ribosome purifications facilitate the efficient analysis of gene expression in *Caenorhabditis elegans* germ cells. *G3.* 10:4063–4069. https://doi.org/10.1534/g3.120.401644

O'Farrell, P.H. 2015. Growing an embryo from a single cell: A hurdle in animal life. *Cold Spring Harb. Perspect. Biol.* 7:a019042. https://doi.org/10.1101/cshperspect.a019042

Perez, M.F., and B. Lehner. 2019. Vitellogenins - yolk gene function and regulation in *Caenorhabditis elegans*. *Front. Physiol.* 10:1067. https://doi.org/10.3389/fphys.2019.01067

Roeder, A.H.K., A. Cunha, C.K. Ohno, and E.M. Meyerowitz. 2012. Cell cycle regulates cell type in the Arabidopsis sepal. *Development*. 139:4416–4427. https://doi.org/10.1242/dev.082925

Sallee, M.D., J.C. Zonka, T.D. Skokan, B.C. Raftrey, and J.L. Feldman. 2018. Tissue-specific degradation of essential centrosome components reveals distinct microtubule populations at microtubule organizing centers. *PLoS Biol.* 16:e2005189. https://doi.org/10.1371/journal.pbio.2005189

Sallee, M.D., M.A. Pickett, and J.L. Feldman. 2021. Apical PAR complex proteins protect against programmed epithelial assaults to create a continuous and functional intestinal lumen. *Elife*. 10:e64437. https://doi.org/10.7554/eLife.64437

Schmoller, K.M., J.J. Turner, M. Kõivomägi, and J.M. Skotheim. 2015. Dilution of the cell cycle inhibitor Whi5 controls budding-yeast cell size. *Nature*. 526:268–272. https://doi.org/10.1038/nature14908

Sen, I., A. Kavšek, and C.G. Riedel. 2021. Chromatin immunoprecipitation and sequencing (ChIP-seq) optimized for application in Caenorhabditis elegans. *Curr. Protoc.* 1:e187. https://doi.org/10.1002/cpz1.187

Swaffer, M.P., J. Kim, D. Chandler-Brown, M. Langhinrichs, G.K. Marinov, W.J. Greenleaf, A. Kundaje, K.M. Schmoller, and J.M. Skotheim. 2021. Transcriptional and chromatin-based partitioning mechanisms uncouple protein scaling from cell size. *Mol. Cell*. 81:4861–4875.e7. https://doi.org/10.1016/j.molcel.2021.10.007

Swaffer, M.P., G.K. Marinov, H. Zheng, L. Fuentes Valenzuela, C.Y. Tsui, A.W. Jones, J. Greenwood, A. Kundaje, W.J. Greenleaf, R. Reyes-Lamothe, and J.M. Skotheim. 2023. RNA polymerase II dynamics and mRNA stability feedback scale mRNA amounts with cell size. *Cell*. 186:5254–5268.e26. https://doi.org/10.1016/j.cell.2023.10.012

Unhavaithaya, Y., and T.L. Orr-Weaver. 2012. Polyploidization of glia in neural development links tissue growth to blood-brain barrier integrity. *Genes Dev.* 26:31–36. https://doi.org/10.1101/gad.177436.111

Uppaluri, S., S.C. Weber, and C.P. Brangwynne. 2016. Hierarchical size scaling during multicellular growth and development. *Cell Rep.* 17: 345–352. https://doi.org/10.1016/j.celrep.2016.09.007

van Rijnberk, L.M., R. Barrull-Mascaró, R.L. van der Palen, E.S. Schild, H.C. Korswagen, and M. Galli. 2022. Endomitosis controls tissue-specific gene expression during development. *PLoS Biol.* 20:e3001597. https://doi.org/10.1371/journal.pbio.3001597

Van Rompay, L., C. Borghgraef, I. Beets, J. Caers, and L. Temmerman. 2015. New genetic regulators question relevance of abundant yolk protein production in C. elegans. *Sci. Rep.* 5:16381. https://doi.org/10.1038/srep16381

Weigert, M., U. Schmidt, R. Haase, K. Sugawara, and G. Myers. 2020. Star-convex polyhedra for 3D object detection and segmentation in microscopy. In 2020 IEEE Winter Conference on Applications of Computer Vision (WACV), IEEE, New Jersey, NY, USA. 3655–3662. https://doi.org/10.1109/WACV45572.2020.9093435

Xie, S., and J.M. Skotheim. 2020. A G1 sizer coordinates growth and division in the mouse epidermis. *Curr. Biol.* 30:916–924.e2. https://doi.org/10.1016/j.cub.2019.12.062

Xiong, R., and K. Sugioka. 2020. Improved 3D cellular morphometry of Caenorhabditis elegans embryos using a refractive index matching medium. *PLoS One*. 15:e0238955. https://doi.org/10.1371/journal.pone.0238955

Yi, Y.-H., T.-H. Ma, L.-W. Lee, P.-T. Chiou, P.-H. Chen, C.-M. Lee, Y.-D. Chu, H. Yu, K.-C. Hsiung, Y.-T. Tsai, et al. 2015. A genetic cascade of let-7-ncl-1-fib-1 modulates nucleolar size and rRNA pool in Caenorhabditis elegans. *PLoS Genet.* 11:e1005580. https://doi.org/10.1371/journal.pgen.1005580

Zeldovich, V.B., C.H. Clausen, E. Bradford, D.A. Fletcher, E. Maltepe, J.R. Robbins, and A.I. Bakardjiev. 2013. Placental syncytium forms a biophysical barrier against pathogen invasion. *PLoS Pathog.* 9:e1003821. https://doi.org/10.1371/journal.ppat.1003821

Supplemental material

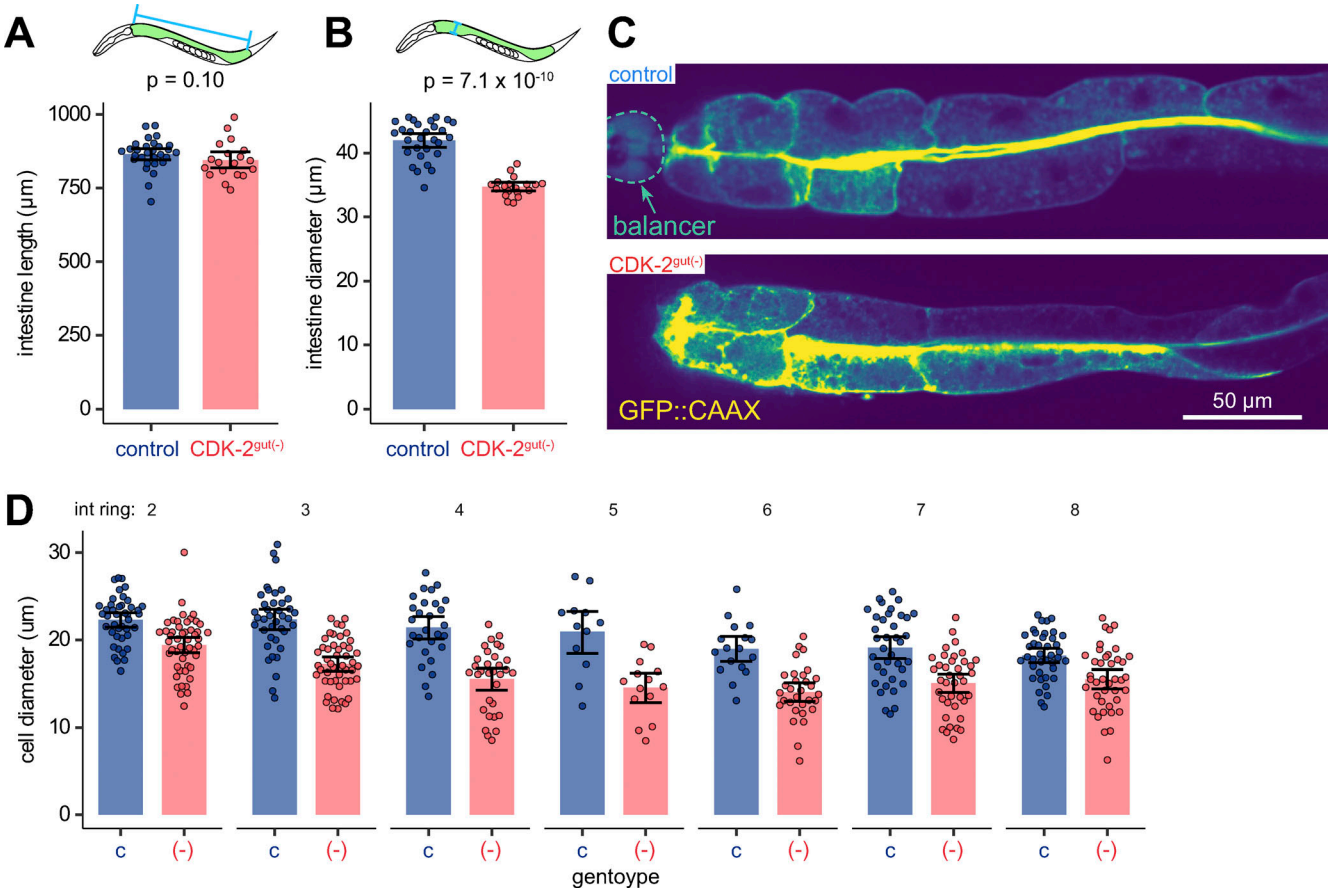

Figure S1. **Extended data used in the calculation of intestinal cell volume. (A and B)** Quantification of intestine length (A) and width (B) from images as in Fig. 1 H. Each point represents one worm; P values are from Mann-Whitney U tests. **(C and D)** To corroborate our organ size measurements, we measured the width of intestinal cells expressing a membrane marker since the width measurement was more sensitive to error in our measurements of bright-field images, such as Fig. 1 H. **(C)** Confocal images of day 2 adult control and CDK-2$^{gut(-)}$ worms expressing *elt-2p::GFP::CAAX* (viridis coloring). **(D)** Quantification of intestine cell width (lumen to the basal surface) from images as in C, grouped by intestinal ring from anterior (int1) to posterior (int8). Each point represents one cell. P = 2.2×10^{-16} for the genotype coefficient in a linear model predicting cell size from genotype and intestinal ring. In all graphs, bars represent means and error bars represent 95% confidence intervals.

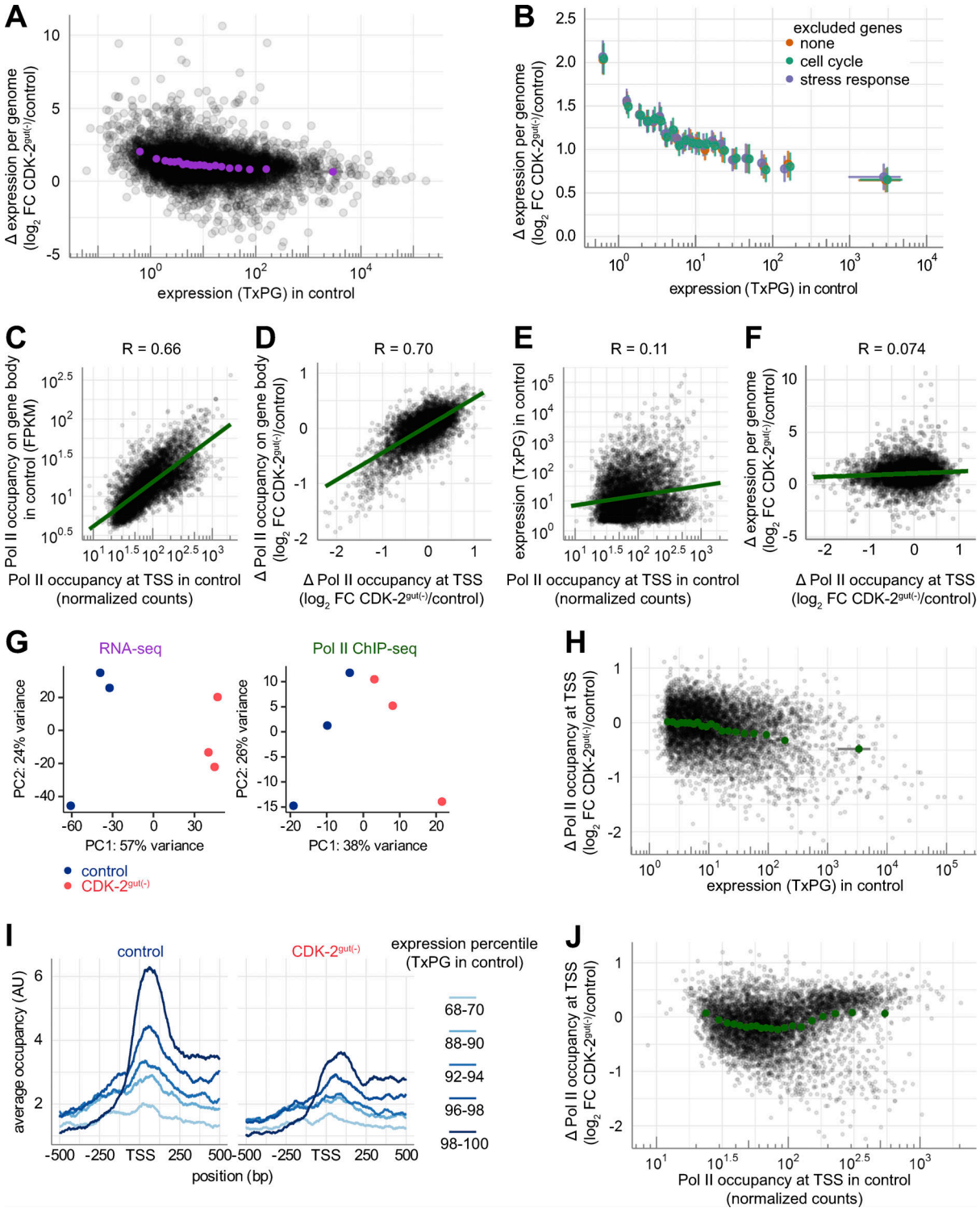

Figure S2. **Extended presentation of RNA-seq and ChIP-seq data. (A)** Full spread of individual genes from RNA-seq along with their binned averages from Fig. 3 C. **(B)** Change in spike-in normalized gene expression (TxPG) plotted against and binned by expression level in control, with and without removal of genes involved in stress response or cell cycle. Each bin represents 5% of genes. Genes were excluded before binning. **(C–F)** Scatter plots comparing different parameters calculated from RNA-seq and Pol II ChIP-seq data sets, as indicated by axes. The occupancy around the transcription start site (TSS) was quantified over a region from 100 bp upstream to 200 bp downstream of the annotated TSS. Each dot represents one gene, lines show best fit linear models. Correlation values are reported above each plot. **(G)** PCA plots of RNA-seq and Pol II ChIP-seq experiments showing variation between biological replicates (dots). **(H)** Full spread of individual genes along with their binned averages from Fig. 3 E. **(I)** Representative metagene profiles showing the average occupancy of a bin of genes at each base pair, relative to the TSS. Each color represents a bin of 2% of genes, binned by their expression level (TxPG) in control, and the height indicates the average Pol II occupancy of genes in the bin. **(J)** Change in Pol II occupancy plotted against and binned by Pol II occupancy in control. Each bin represents 5% of genes, colored dots represent mean fold change within the bin, and error bars represent a 99% confidence interval.

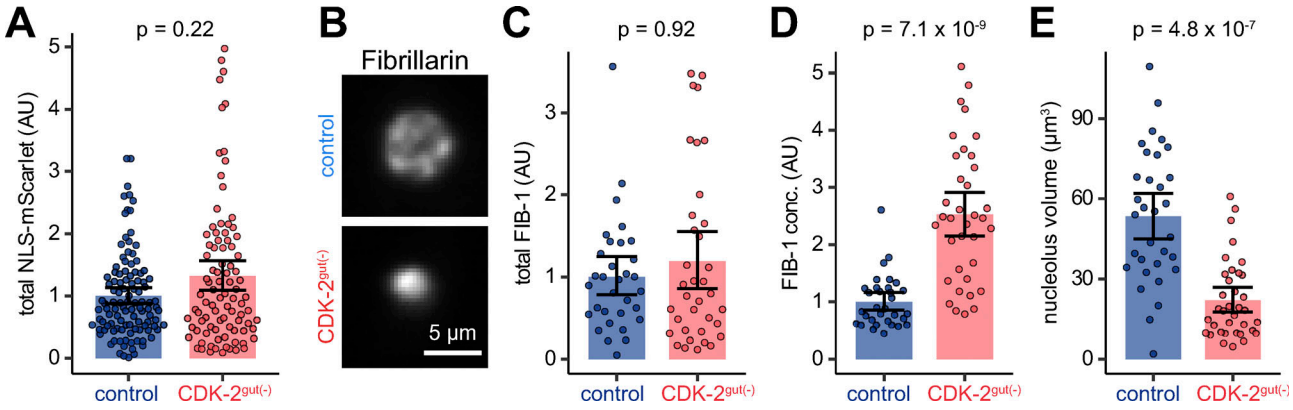

Figure S3. **Quantification of the abundance of a model protein, nucleolus volume, and FIB-1 abundance. (A)** Quantification of total fluorescence intensity in intestinal nuclei from confocal images of day 2 adult worms expressing a single copy transgene, *asp-1p::NLS-mScarlet*. **(B)** Live confocal images of intestinal nucleoli of day 1 adult worms expressing endogenously-tagged Fibrillarin (wrmScarlet11::FIB-1) and ubiquitous *eft-3p::wrmScarlet1-10*, reconstituting fluorescently-tagged Fibrillarin only in the intestine. **(C–E)** Quantification of the total amount (C, total fluorescence intensity), concentration (D, mean fluorescence intensity) and volume (E), of FIB-1. In A and C–E, each dot represents one nucleus or nucleolus, bars and error bars represent means and 95% confidence intervals, and P values are from Mann-Whitney U tests after Benjamini-Hochberg multiple hypothesis testing correction.

Provided online are Table S1, Table S2, Table S3, Table S4, Table S5, Table S6, Table S7, and Table S8. Table S1 details specific nematode strains and genotypes used in each experiment. Table S2 details genetic alleles used in this study. Table S3 details plasmids used in this study. Table S4 details oligos used in this study. Table S5 contains calculated values from the RNA-seq experiment. Table S6 contains GO term 1D enrichment scores from the RNA-seq experiment. Table S7 contains calculated values from the ChIP-seq experiment. Table S8 contains GO terms that were used in this study and associated gene names.